University of Potsdam

– Institute of Earth and Environmental Science –

Validation of Digital Elevation Models (DEMs) & Derived Geomorphic Metrics on the Southern Central Andean Plateau

Master's Thesis

by

Benjamin Purinton

(Student-ID: 778174)

In partial fulfillment of the requirements for the degree of

Master of Science (M.Sc.)

Advisor: Prof. Dr. Bodo Bookhagen

Co-advisor: Dr. Wolfgang Schwanghart

Berlin

October 12, 2016

Abstract

Geomorphologists use digital elevation models (DEMs) to quantify topography – often without rigorous accuracy assessments. In this study we compare the elevation accuracy and geomorphometric application of the current generation of global 30 m DEMs (SRTM C-band, ASTER GDEM2, and ALOS World 3D), a regional 30 m DEM generated from eight stacked ASTER L1A stereopairs, three regional 10 m DEMs generated from TerraSAR-X / TanDEM-X radar pairs, and a regional 5 m DEM (ALOS World 3D). Additional regional 5-12 m DEM generation from optical satellite data (SPOT6 scenes, RapidEye scenes, and ALOS PRISM tri-stereopair) were attempted but unused due to remaining noise in slope and curvature calculations. Our study focuses on the southern Central Andean Plateau, where diverse topography, lack of vegetation, and clear skies create ideal conditions for remote sensing. Further, tectonic activity in this region has generated relevant features for a tectonic geomorphology analysis. We assessed vertical accuracy by comparing standard deviations (SD) of the DEM elevation versus a control dataset of > 300,000 differential GPS (dGPS) measurements with < 0.5 m elevation accuracy across 4,000 m of elevation. The May 2016-released global ALOS World 3D has the highest accuracy of the 30 m DEMs with SD = 2.81 m, outperforming the SRTM C-band at 3.33 m. The ALOS World 3D and SRTM-C display no apparent vertical biases related to elevation, slope, or aspect, but there are few measurements on slopes > 30º. The lower quality of the ASTER GDEM2 is apparent with a SD = 9.48 m and an aspect related bias with an amplitude of ~5 m repeating at ~65º, ~135º, ~195º, and ~325º. Through weighted stacking of eight manually generated 30 m ASTER L1A stereopair DEMs, we display an improvement in accuracy to SD = 6.93 m. The 10 m TerraSAR-X / TanDEM-X DEMs have SD = 2.02-3.83 m and the 5 m ALOS World 3D has SD = 1.64 m. In a second analysis step, we compare geomorphic metrics derived from a 30 m (SRTM-C), 10 m (TerraSAR-X / TanDEM-X), and 5 m (ALOS World 3D) DEM focused on a 66 km^2 catchment with a clear river knickpoint. For trunk channel profiles analyzed with chi plots, consistent *m/n* values of 0.51-0.57 are found regardless of DEM resolution, SD, or chi plot method. Hillslopes are analyzed upstream and downstream of the knickpoint by calculating slope and curvature distributions and plotting slope, curvature, and drainage area. While relief and slope measurements vary little between datasets, accurate hillslope lengths require higher resolution 5 m data. Curvature variability is also only captured by the 5 m data, however, attempts at analyzing sub-basin morphological variability with respect to the dynamic knickpoint feature are hampered by complex basin morphology and an inability to capture fine-scale ridge-crest curvature changes. The improvements in accurate high resolution satellite data for geomorphometric analysis are promising, but higher-resolution lidar data is still necessary for fine-scale analysis.

Zusammenfassung

In dieser Studie vergleichen wir die Höhengenauigkeit und die geomorphologische Eignung der gängigen Generation von: 1) globalen 30 m DHM (SRTM C-band, ASTER GDEM2, und ALOS World 3D); 2) einem aus 8-fach gestapelten ASTER L1A Stereopaar generiertem regionalen 30 m DHM; 3) drei aus dem TerraSAR-X / TanDEM-X Radar Paar generiertem regionalen 10 m DHM; und 4) einem regionalen 5 m DHM (ALOS World 3D). Die Generierung weiterer regionaler 5-12 m DHM aus optischen Satelliten Daten (SPOT6 Szene, RapidEye Szene und ALOS PRISM tri-stereopaar) ergab mit Rauschen versetzte Daten, welche bei der weiterer Prozessierung ausgeschlossen wurden. Der Fokus dieser Studie liegt auf der südlichen Hochebene der Zentral Anden, wo tektonische Aktivität zur kennzeichnender Geomorphologie führte, die es zu untersuchen gilt. Das Zusammenspiel von topographischer Diversität, spärlicher Vegetation, sowie überwiegend klaren Himmel bildet ein optimales Set für Fernerkundung. Die vertikale Genauigkeit wurde erreicht durch das Vergleichen der Standardabweichung (SD) der DHM-Höhe mit einem Kontrolldatenset von > 300.000 differentiellen GPS (dGPS) Punktmessungen, aufgenommen über 4.000 Höhenmetern verteilt. Das im Mai 2016 veröffentlichte globale ALOS World 3D hat die höchste Genauigkeit im 30 m DHM Bereich mit einer SD = 2,81 m, was die 3,33 m des SRTM C-band unterbietet. Die ALOS World 3D und SRTM C-band weisen keine vertikalen Fehler auf, weder in Höhe, Steigung noch in Fallrichtung. Die untere Qualitätsgrenze der ASTER GDEM2 ist vergleichbar mit einer SD = 9,48 m und einem vom Einfallen beeinflussten Bias mit einer Amplitude von ~5 m. Durch gewichtete Stapelung von acht manuell generierten 30 m ASTER L1A Stereopaar DHM, konnte eine Erhöhung der Genauigkeit auf SD = 6,93 m erreicht werden. Die 10 m TerraSAR-X / TanDEM-X DHM haben eine SD im Bereich von 2,03-3,83 m und das 5 m ALOS World 3D eine SD = 1.64 m. In einem zweiten Analyseverfahren wurden geomorphologische Parameter aus dem 30 m (SRTM-C), 10 m (TerraSAR-X / TanDEM-X) und 5 m (ALOS World 3D) DHM verglichen, aus einem 66 km^2 großem Einzugsgebiet mit einem eindeutigen Gefällsbruch im Flussverlauf. Chi-Plot Analysen von Flussbett Profilen ergaben konstante *m/n* Werte im Bereich von 0.51-0.57, unabhängig von der DHM Auflösung, der SD, sowie der Chi-Plot Methode. Die Hangneigung wurde Flussabwärts und -aufwärts vom Gefällsbruch durch Bestimmung der Neigungs- und Krümmungsverteilung bestimmt, sowie durch das Plotten von Neigung, Krümmung und des Einzugsgebietes. Messungen von Relief und Neigung variieren innerhalb unterschiedlicher Datensätze. Für eine präzise Bestimmung der Hangneigungslänge wären höher aufgelöste 5 m Daten benötigt gewesen. Variationen in den Krümmungswerten konnten nur in Bereich der Daten aus dem 5 m Datenset beobachtet werden. Ansätze zur Analyse von morphologischen Varietäten im Sub-Becken Bereich in Abhängigkeit von dynamischen Gefällsbruch Eigenschaften sind aufgrund komplexer Beckenmorphologie und eingeschränkter Erfassung von Bergrückenkrümmungsunterschieden im Fine-Scale Bereich gescheitert. Obwohl eine Verbesserung der Genauigkeit von hochauflösenden Sateliten Daten für geomorphologische Analysen vielversprechend sind, kann eine Fine-Scale-Anaylse nur mit Hilfe von hochauflösenden LIDAR Daten durchgeführt werden.

Contents

1. Introduction

The proliferation of digital elevation models (DEMs) for topographic analysis in the past twenty years has provided geomorphologists with powerful tools to explore the linkages between fundamental geomorphic processes and landforms and to test hypotheses of landscape evolution at local and regional scales using geomorphic metrics (e.g., Howard et al., 1994; Burbank et al., 1996; Whipple and Tucker, 1999; Montgomery et al., 2001; Dietrich et al., 2003; Roering et al., 2007). Modern geomorphologists use the quantitative sub-discipline of geomorphometry (Pike et al., 2009) to explore how tectonic, climatic, and lithologic signals can be inferred from DEMs; particularly how a basin's transient adjustment to changing climatic (e.g., increased precipitation) or tectonic (e.g., baselevel fall) boundary conditions are recorded in topography (e.g., Snyder et al., 2000; Wobus et al., 2006; DiBiase et al., 2010; Bookhagen and Strecker, 2012; Kirby and Whipple, 2012; Scherler et al., 2015; Clubb et al., 2016; Olen et al., 2016). Questions remain to what extent transient responses can be recorded in landscape morphology sampled from a DEM at the scale of catchments to mountain ranges (e.g., DiBiase et al., 2010; DiBiase et al., 2012; Olen et al., 2016), and how the morphology of channel networks and hillslopes can independently act as records of basin transience used to map erosion rates (e.g., Wobus et al., 2006; Ouimet et al., 2009; Kirby and Whipple, 2012; Hurst et al., 2012; Clubb et al., 2016; Forte et al., 2016; Olen et al., 2016). The discrete parameterization of the land surface using elevation and its derivatives (e.g., slope, curvature, aspect) calculated from DEMs is a necessary step for the extraction of geomorphic features. Therefore, hillslope and channel analysis requires accurate DEMs, as errors will propagate and grow in the first (slope) and second (curvature) derivatives of elevation, potentially obscuring geomorphic metrics (Reuter et al., 2009; Wilson, 2012).

Remotely sensed DEMs – we refer to all digital topography herein as DEMs, as opposed to the often used term digital terrain model (DTM) for bare-earth models with vegetation and structures removed – are generated from data that are originally distorted through sensor, terrain, and atmospheric conditions leading to misrepresentations (error) in the final product (Smith and Sandwell, 2003; Fisher and Tate, 2006; Nuth and Kääb, 2011). Because of this, height

error reporting using a control dataset is an important, and often neglected, step before application of DEMs to geomorphic studies (Fisher and Tate, 2006; Wechsler, 2007). Additionally, DEMs are typically received as gridded datasets with a defined measurement interval (resolution) that may oversimplify fine landscape variability, so consideration must also be taken of the geomorphic scales of interest (e.g., Hengl, 2006). For instance, while channel profiles over long reaches are readily analyzed on coarser 90 m resolution data, hillslopes with considerably smaller extents require higher 1-30 m resolution data capable of identifying individual hillslopes and ridge-crests. Furthermore, DEM biases specific to a given sensor should be considered prior to analysis, especially in steep topography (e.g., Nuth and Kääb, 2011).

Since the release of the first global DEM by the United States Geological Survey (USGS) in 1996 (GTOPO30) at a resolution of 30 arc-seconds (~1 km), advances in remote sensing technology – particularly satellite observation – and processing capabilities have steadily improved the accuracy and reduced the resolution of DEMs. The 2003 release of the 90 m Shuttle Radar Topography Mission (SRTM) global DEM ushered in a new age of geomorphometry (Pike et al., 2009). With the 2009 release of the 30 m Advanced Spaceborne Thermal Emission and Reflection Radiometer Global DEM (ASTER GDEM; METI/NASA/USGS, 2009), and more recent releases of the improved ASTER GDEM version 2 (ASTER GDEM2; Tachikawa et al., 2011), SRTM C-band 30 m (SRTM-C), and up-sampled Advanced Land Observing Satellite (ALOS) World 3D 30 m (AW3D30), geomorphologists now have open access to many large-scale DEMs. In addition to these public 30 m global datasets, higher resolution (1-10 m) regional DEMs from a variety of satellite sources are becoming increasingly available through commercial purchase as edited products (e.g., ALOS World 3D and TerraSAR-X / TanDEM-X WorldDEM), optical stereopairs for stereogrammetric processing (e.g., Pleiades-1A and ALOS PRISM), and radar scenes for interferometric processing (e.g., TerraSAR-X / TanDEM-X).

The global SRTM-C and ASTER GDEM2 have reported vertical accuracies of ~5-20 m depending on terrain characteristics (e.g., Mukherjee et al., 2013; Rexer and Hirt, 2014), with some biases reported related to slope and aspect of

6

the terrain (e.g., Berthier et al., 2006; Nuth and Kääb et al., 2011; Shortridge and Messina, 2011). While these accuracies allow long-term (decadal) tracking of glacial elevation changes (e.g., Racoviteanu et al., 2007; Paul and Haeberli, 2008), higher resolution regional DEMs from optical and radar sources have proven more accurate (< 5 m vertical error) than these global products for glacial studies in steep terrain, particularly on shorter time scales (e.g., Berthier et al., 2007; Berthier and Toutin, 2008; Jaber et al., 2013; Neckel et al., 2013; Pandey and Venkataraman, 2013; Holzer et al., 2015; Rankl and Braun, 2016; Neelmeijer et al., in review). However, to date no studies have assessed the accuracy of the current generation of high-resolution, satellite-derived DEMs with regards to geomorphometry. These measurements, unlike glacial studies, rely on the derivatives of elevation (e.g., slope and curvature) and not the absolute height or height changes. Furthermore, glacial studies are typically conducted on lower slope terrain and compare area-wide measurements allowing the averaging out of some error. On the other hand, geomorphic studies examining channels and hillslopes in steeper terrain may be more impacted by remote-sensing errors and artifacts (e.g., from shadowing), and geomorphic parameters rely on the accuracy of a single pixel and its relation to the surrounding pixels.

Recently, the application of light detection and ranging (lidar) by ground and aerial methods has been applied to generate meter to sub-meter scale elevation point clouds and gridded DEM datasets at smaller areal extents than satellite derived DEMs (Passalacqua et al., 2015). Lidar has revolutionized geomorphology with more accurate representations of the land surface and led to new insights and discoveries in the realm of mass and energy transport laws, channel initiation, surface flow routing, and landslide and fault scarp mapping (e.g., Dietrich et al., 2003; Roering et al., 2007; Roering et al., 2013; Shelef and Hilley, 2013; Tarolli, 2014). Furthermore, previous studies examining the effect of grid resolution on geomorphic metrics have primarily used resampled lidar data (e.g., Tarolli and Tarboton, 2006; Tarolli and Dalla Fontana, 2009; Grieve et al., 2016c).

While coarser DEMs have proven useful in exploring mountain belt hypsometry and linkages between climate, erosion, and tectonics at basin or

regional scales (e.g., Montgomery et al., 2001; DiBiase et al., 2010; Bookhagen and Strecker, 2012), their utility in analyzing process-level geomorphology and assessing critical hillslope parameters is limited and lidar is often deemed necessary (Tarolli and Tarboton, 2006; Tarolli and Dalla Fontana, 2009; Tarolli, 2014; Roering et al., 2007; Passalacqua et al., 2015). Despite this, the limited spatial extent (~1 km^2) and high effort and cost of obtaining lidar are prohibitive factors to its application at basin or regional scales (10-1,000 km^2). Advances in high-resolution (1-10 m) regional DEM availability and accuracy from a number of satellites have proven useful to studies of glacial and volcanic elevation change (e.g., Holzer et al. 2015; Bagnardi et al., 2016), however, investigation of their advantages over 30 m public DEMs in representing derivatives of elevation for channel and hillslope analysis in lieu of lidar is still necessary.

This study shows a multi-DEM validation for the southern Central Andes in NW Argentina in an arid landscape with no vegetation cover, ideal for remote sensing. DEM validation is presented by: (i) reporting the vertical accuracy of a number of global and regional remotely sensed DEMs at resolutions of 5, 10, and 30 m from open access portals, commercial sources, and research agreements; and (ii) carrying out channel profile and hillslope geomorphometric analysis for a 66 km^2 catchment with a clear knickpoint to assess the representation of elevation gradients and the quality of these DEMs for tectonic geomorphology.

2. Study Area

The present study centers on the Puna de Atacama plateau in northwest Argentina (Fig. 1A). The Puna is the southern extension of the low relief, high elevation, internally drained Central Andean Plateau (also referred to as the Altiplano-Puna Plateau), extending for over 1,500 km and reaching widths of over 350 km in the Central Andes (Allmendinger et al., 1997). Due to the plateau's hyper-arid climate caused by orographic blocking and regional atmospheric circulation patterns (Bookhagen and Strecker, 2008; Rohrmann et al., 2014), there is an absence of cloud and vegetation cover on the Puna, creating ideal conditions for remote sensing of the bare-earth surface. As the Puna is largely uninhabited and erosion rates are very low (e.g., Bookhagen and Strecker, 2012), the study site is a pristine environment experiencing little change from year-to-year, thus minimizing differences between DEMs collected years apart. Topographic expression is diverse on the plateau with flat salars having near-zero relief at 5-10 km scales surrounded by steep volcanoes and mountain ranges with > 2 km of relief at 2-5 km scales. This morphology is readily apparent around the Pocitos Basin, centered on the Salar de Pocitos (elevation ~3,600 m) and bordered by mountains such as the Nevado Queva reaching elevations of over 6,000 m (Fig. 1B). Within the Pocitos Basin, we focus geomorphometric analysis on the 66 km^2 Quebrada Honda catchment, with 1.2 km of relief (Fig. 1C). The Quebrada Honda was chosen for geomorphic comparisons for its coverage across available DEMs, size, uniform Paleozoic metasedimentary lithology, and the presence of a knickpoint 7 km upstream of the outlet that divides the basin into transiently adjusting sections.
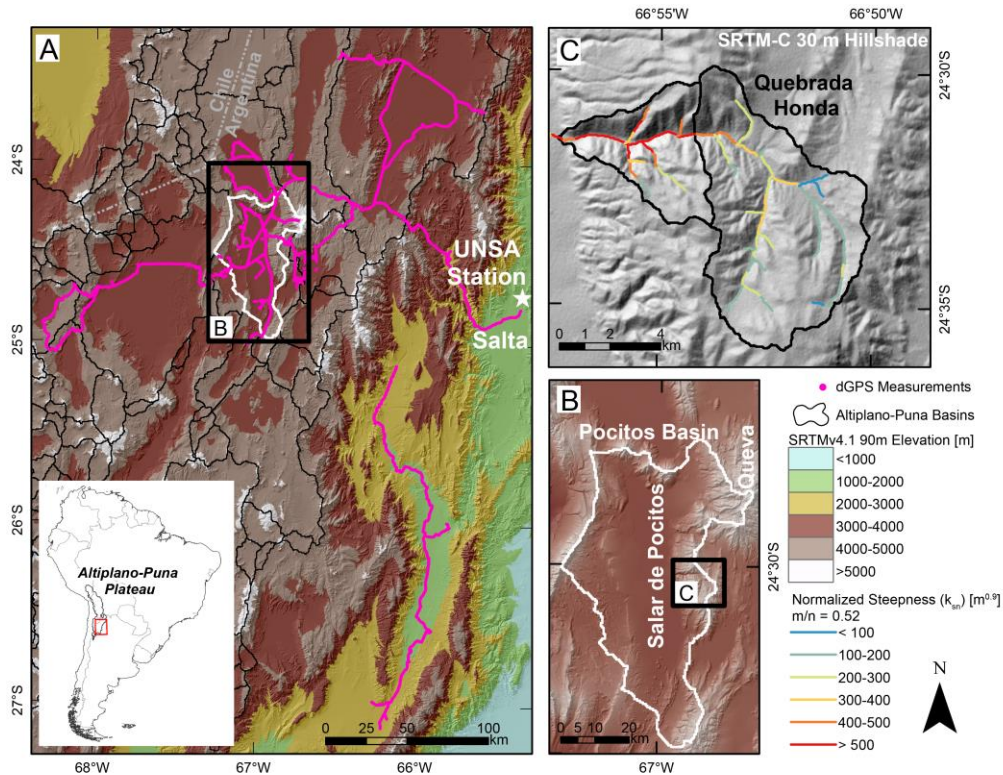
Figure 1. (A) Topographic overview of the South American study area. 307,509 dGPS measurements displayed in pink. UNSA base station (white star) for dGPS kinematic correction located in Salta, Argentina. Inset shows South American continent with international borders and internally-drained Central Andean Plateau (Altiplano-Puna). Study focus is the Pocitos Basin (B), where elevation ranges from 3,600 m on the flat salar to 6,000 m on surrounding peaks. Geomorphometric analyses focus on the Quebrada Honda (C) catchment draining an area of 66 km^2 from 5,000 m of elevation down to 3,800 m. A knickpoint 7 km upstream divides the basin into an upper and lower section with differing morphology (Fig. 2). The transition is observable along the trunk as normalized channel steepness (k_{sn}) averaged along 300 m reaches on the SRTM-C 30 m DEM increases to values > 500. The *m/n* reference value of 0.52 is calculated using chi plot analysis. Elevations in (A) and (B) are from the 90 m SRTMv4.1 DEM (Jarvis et al., 2008).

10

3. Data and Methods

3.1. dGPS Data

Vertical accuracy of optical and radar DEMs was assessed using a unique high-accuracy differential GPS (dGPS) dataset spanning 4,000 m of elevation centered on the Pocitos Basin (Fig. 1A). Of 333,555 total raw dGPS measurements collected during field campaigns from March 2014-2016, 307,509 kinematically corrected points with vertical and horizontal accuracies < 0.5 m were selected for the final control on DEM vertical accuracy. Data were projected to the EGM96 vertical and WGS84 horizontal datums in the UTM coordinate system zone 19S. This point measurement dataset was rasterized to the resolution and extent of each DEM. Multiple measurements within a DEM pixel were averaged and pixels without measurements were set to no data. This led to a reduction in the number of individual measurements used to assess DEM vertical accuracy, but accounted for multiple measurements per pixel to provide a robust validation. Details of measurement collection and post-processed kinematic correction of the raw dGPS files using the UNSA permanent station in Salta (Fig. 1A) can be found in Appendix A.

3.2. DEM Datasets

DEMs collected from a number of public, commercial, and research agreement sources are listed in Table 1. All were referenced to the same datums (EGM96 / WGS84) and projected into UTM19S using bilinear interpolation. All DEMs were co-registered to a common control – the SRTM-C, selected for its excellent geolocation accuracy (Rodriguez et al., 2006) – using affine parameters by up- or down-sampling the SRTM-C to the resolution of the DEM of interest and iteratively shifting to reduce the root mean squared error (RMSE) of the elevation difference. This step insures all DEMs are aligned and allows direct comparisons of elevation between them (e.g., Nuth and Kääb, 2011). Additional information on each dataset listed in Table 1 are found in Appendix B, including datasets that were not included in the comparison due to lower DEM resolution or quality issues (SRTMv4.1 90 m, SRTM-X 30 m, RapidEye

12 m, SPOT6 5 m, ALOS PRISM tri-stereopair 10 m, TerraSAR-X pairs 10 m, and TerraSAR-X / TanDEM-X pairs processed to 5 m).

Table 1. List of DEMs used for comparison and geomorphic analysis.

Dataset (short name)	Data Type	Resolution (m)	Source	Notes
SRTM C-band (SRTM-C)	Radar / Edited global product	30	Public / https://lta.cr.usgs.gov/SRTM1Arc	Released 2014, previously only US coverage
ASTER GDEM Version 2 (ASTER GDEM2)	Optical / Edited global product	30	Public / https://asterweb.jpl.nasa.gov/gdem.asp	Released 2011, update of ASTER GDEM1 released 2009
ASTER L1A Stereopair Stack (ASTER Stack)	Optical / Raw stereopairs	30	Public / http://reverb.echo.nasa.gov/reverb/	ASTER GDEM2 was generated by automated processing and stacking of these original stereopairs
ALOS World 3D 30 m (AW3D30)	Optical / Edited global product	30	Public / http://www.eorc.jaxa.jp/ALOS/en/aw3d30/	Released May 2016, down-sampled version of commercial DEM product
ALOS World 3D 5 m (AW3D5)	Optical / Edited global product	5	Commercial / http://aw3d.jp/en/	Released 2015 as highest resolution commercial global DEM
TerraSAR-X / TanDEM-X (TSX/TDX)	Radar / Raw interferograms	10	Research agreement / http://terrasar-x.dlr.de/	TanDEM-X and TerraSAR-X mission were used to generate the commercial 12 m WorldDEM in 2015

3.3. ASTER Stacking

The ASTER radiometer has collected along-track stereopairs with nadir (Band 3N) and backward (Band 3B) looking near infrared cameras between 83º N and 83º S since 1999 (Tachikawa et al., 2011). Using these stereopairs, a 30 m ASTER global DEM has been generated by automatic stereo-correlation, stacking, and averaging of over 1.2 million scenes. The 2011 release of the ASTER GDEM version 2 (ASTER GDEM2) used in the present study

represented a vast improvement in quality (Tachikawa et al., 2011), however remaining noise is caused by issues with cloud cover, water masking, the smaller stereo correlation kernel, and mis-registration of scenes prior to stacking (Nuth and Kääb, 2011). We seek to improve on the ASTER GDEM2 using eight raw ASTER L1A 3N/B stereopairs downloaded with variable overlap from the Pocitos Basin. Using stereogrammetric processing methods we generated eight 30 m DEMs from these stereopairs. Details of DEM generation along with RMSE of ground control and tie points are presented in Appendix B (Table B1). Each L1A DEM was co-registered to the SRTM-C, manually masked for outliers showing abrupt hundreds to thousands of meters steps in elevation (caused by clouds or haze in the imagery or software processing errors), and differenced with the SRTM-C. Pixels were weighted with a bi-square scheme based on their correlation with the SRTM-C, and a weighted average of the overlapping DEMs was used to generate a higher quality 30 m ASTER Stack.

3.4. Elevation Accuracy Assessment

To assess DEM vertical accuracy, we first performed a pixel-by-pixel comparison of rasterized dGPS and DEM elevation values after co-registration to the SRTM-C. As our dGPS data have vertical uncertainties (< 0.5 m) below the elevation intervals of all available DEMs, they are taken as an absolute control. Our preferred metric for DEM vertical accuracy is the mean $\pm$ 1-sigma (σ) standard deviation (SD) (Li, 1988; Fisher and Tate, 2006). Specifically, we are interested in the SD of DEM elevation versus dGPS height as our quality metric. Plotted histograms of uncertainty distribution were normalized by their respective mean offsets so the SD could be visually compared. Differences of ± 30 m were filtered out as outliers caused by bad data and processing errors, and the percentage reduction in number of measurements from this filtering is reported as an additional quality check. In a second step, we examined error distributions with respect to terrain slope, aspect, and elevation for the wide-coverage 30 m global DEMs (SRTM-C, ASTER GDEM2, and AW3D30), in which case we also normalize by mean offset, but did not exclude ± 30 m outliers. Measurements are separated into 100 m elevation bins ranging from

1,100 m in the foreland to 5,000 m on the peaks surrounding the Pocitos Basin (Fig. 1A). Slopes are binned by 1°, up to a maximum of 45° for the ASTER GDEM2 and SRTM-C and 42° for the AW3D30. Aspect is binned by 10° with north at 0° and east at 90°. Vertical uncertainty is plotted in each bin as a box plot showing the median, 25-75th percentile range, and 1st and 99th percentile outlier cutoffs.

3.5. Geomorphometric Analysis

We go beyond pixel-by-pixel vertical accuracy comparisons by examining channel and hillslope parameters extracted from these DEMs in order to assess their representation of derivatives of elevation and as well as the improvements from 30 m (SRTM-C) to 10 m (TSX/TDX) to 5 m (AW3D5) spatial resolutions. The derivation of geomorphic metrics relies on accurate landscape representation by the DEMs, thus providing a relative assessment of their quality in complement to the elevation validation by dGPS. We focus on the 66 km^2 Quebrada Honda (Fig. 2), and exploit the transient setting resulting from the knickpoint by separating analyses between downstream steep and upstream gentle-sloped terrain. This allows us to test hypotheses of hillslope morphology adjustment to different river gradients in a large catchment with the same climatic and lithologic conditions. The size of the catchment necessitates large-coverage, remotely sensed DEMs, whereas lidar data would be difficult to attain and expensive for a catchment of this size.
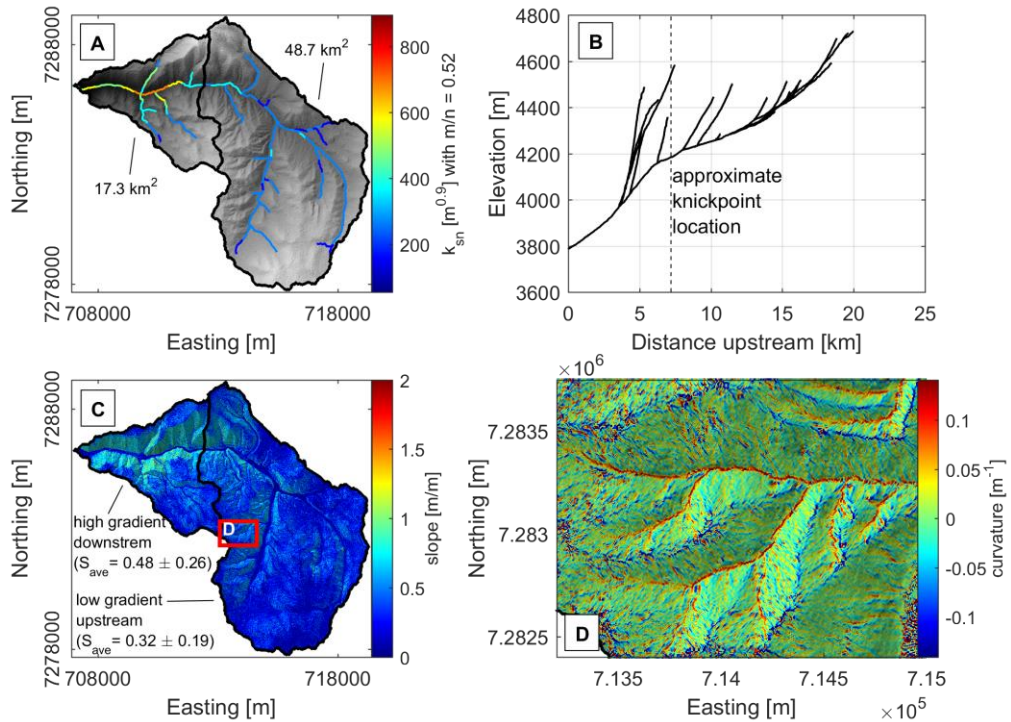
Figure 2. Topographic overview of Quebrada Honda (cf. Figure 1) from commercial AW3D5 5 m DEM. Coordinates in UTM zone 19S. (A) Normalized channel steepness (k_{sn}) averaged over 300 m reaches using $m/n = 0.52$ with upstream and downstream drainage areas indicated by black outlines. All tributaries with drainage area > 1 km^2 are plotted. (B) Longitudinal profile of trunk channel and tributaries with approximate lip of knickpoint indicated. Note the steeper tributaries downstream of the knickpoint. (C) D∞ slope map (Tarboton, 2005) displaying steeper topography downstream of knickpoint, indicated by warmer colors and greater average slope (S_{ave} = mean $\pm$ SD), with area in (D) outlined in red. (D) Curvature colored by ± 2-σ range with positive values concave (channels and valleys) and negative values convex (ridge-crests and hillslopes). Note the positive increase in concave curvature values at channel heads. The variability in convexity and concavity of hillslopes captured in the 5 m DEM is likely related to small scale hillslope processes (e.g., slumps). See Appendix D (Fig. D1) for curvature comparison between DEMs.

3.5.1. Channel Profile Analysis

Advances in longitudinal channel profile analysis driven by accurate DEMs have elucidated changes in boundary conditions recorded in channel slope and upstream propagating knickpoints (e.g., Wobus et al., 2006; Kirby and Whipple, 2012). The stream power incision model (SPIM) of landscape evolution provides the theoretical basis for relating channel slope and drainage area [see Kirby and Whipple (2012) or Lague (2014) for background and limitations of

SPIM]. Applied to a channel profile in steady state ($dz/dt = 0$) we find the relationship:

$$S_C = \left(\frac{U}{K}\right)^{\frac{1}{n}} A^{\frac{-m}{n}} \tag{1}$$

where U is uplift, K is erodibility, A is local drainage area, S_C is local channel slope, and m and n are site-specific constants.

Through an empirical power-law relationship for steady state streams, local channel slope and contributing upstream drainage area are related by (Hack, 1957; Flint, 1974):

$$S_C = k_s A^{-\theta} \tag{2}$$

where the power-law coefficient is channel steepness (k_s) and the power-law exponent is the concavity index (θ). Through equations (1) and (2) we observe that $k_s = (U/K)^{1/n}$ and $\theta = m/n$. Linear regression on plots of log-binned area versus average slope can be used to estimate these constants, and deviations from this logarithmically linear relationship can indicate knickpoints (Kirby and Whipple, 2012). θ, or m/n, values fall in a restricted range (approximately 0.35-0.65), so a reference concavity is often selected to calculate the normalized channel steepness index (k_{sn}) that can be compared across different-sized drainage areas (Wobus et al., 2006). As slope-area regression requires calculation of slope from noisy DEMs, Perron and Royden (2013) recently developed the method of chi plot river profile analysis, which forgoes the need to calculate slope through integration of equation (1) and the introduction of a reference drainage area (A_0) to arrive at:

$$z(x) = z(x_b) + \left(\frac{U}{KA_0^m}\right)^{\frac{1}{n}} \chi \tag{3a}$$

where

$$\chi = \int_{x_b}^{x} \left(\frac{A_0}{A(x)}\right)^{\frac{m}{n}} \tag{3b}$$

In this equation z (elevation) is the dependent variable and χ (integral of drainage area along profile distance) is the independent variable, where x_b is the downstream baselevel start of integration. Channel profiles can be plotted

linearly in chi space by estimating *m/n* using least-squares fitting and selection of the value with the highest R^2 correlation coefficient (Perron and Royden, 2013). This empirical value for *m/n* (θ_{ref}) can then be used to calculate steepness indices (k_{sn}) from equation (2) for mapping patterns of deformation, climatic influence, and/or lithologic boundary conditions (e.g., Forte et al., 2016).

Here, we applied the least-squares R^2 maximization of Perron and Royden (2013) to the 30, 10, and 5 m DEMs for the Quebrada Honda trunk stream (Schwanghart and Scherler, 2014). This method attempts to linearize the entire channel to one best-fit line in chi space and does not provide robust uncertainty estimates for *m/n*, as linear regression is performed through serially correlated values of chi distance and elevation (Perron and Royden, 2013). Because of this, we also employed the piece-wise fitting *m/n* selection algorithm developed by Mudd et al. (2014). This method balances goodness-of-fit for the piece-wise fit profile with model complexity (number of parameters and segments) to provide an *m/n* at the minimum corrected Akaike information criterion (*AICc*) (Akaike, 1974; Hurvich and Tsai, 1989). A SD (uncertainty) of this minimum *AICc* is also provided, over which *AICc* values falling within the SD range indicate other plausible *m/n* values (Mudd et al., 2014). Sensitivity tests were performed by varying fitting parameters with final parameters (and example plots for both methods) reported in Appendix C.

3.5.2. Hillslope Geomorphic Metrics

Besides channel profile analysis, signals of denudation and uplift may also be inferred from hillslope morphology as determined by geomorphic metrics including hillslope length, relief, slope angles, and curvature. These parameters calculated from DEMs also allow the exploration of empirical geomorphic transport laws (cf. Dietrich et al., 2003). Further, the accurate sampling of local relief (*R*), slope angles (*S*), and curvatures (*C*) allows patterns of erosion to be mapped from topography alone (e.g., DiBiase et al., 2010; Hurst et al., 2012).

Characteristic hillslope length (L_H) is a horizontal measure of the hillslope-to-valley transition, demarcated by the first inflection in slope-area plots at a critical drainage area where channel heads are able to initiate (e.g., Tarolli and

Dalla Fontana, 2009). Early studies making use of contour map derived DEMs displayed their utility in exploring the hillslope-to-valley transition via contributing area-slope relationships, but only given a fine enough resolution ($\leq$ 30 m) to observe the slope-area inflection (Montgomery and Foufoula-Georgiou, 1993; Zhang and Montgomery, 1994; Ijjasz-Vasquez and Bras, 1995). Dividing the critical drainage area by the unit contour width (in a wider sense DEM resolution) then provides an approximation of L_H (e.g., Roering et al., 2007). Slope-area plots provide a measure of L_H in the horizontal sense, measured from ridge-crest to channel margin, which can be used to compare different landscape settings (e.g., Henkle et al., 2011; Grieve et al., 2016a).

The distributions of slope and curvature measured on a DEM have been demonstrated to increase with increasing resolution, leading to differences in geomorphometric analyses (e.g., Vaze et al., 2010; Grieve et al., 2016c). Generally, higher resolution DEMs are necessary to explore process level geomorphology reliant on local slope and curvature measurements (e.g., Tarolli, 2014), whereas basin averaged slopes measured on 10 m resolution DEMs have been shown to follow patterns of erosion up to a limiting value (DiBiase et al., 2010). On the other hand, hilltop curvature (C_{HT}) mapped from high resolution lidar DEMs has been demonstrated to follow patterns of erosion well beyond the hillslope and channel limits (Hurst et al., 2012). Despite this, it has been suggested that at resolutions $\geq$ 5 m, DEMs are unable to capture the fine variability of these curvature measurements (e.g., Clubb et al., 2016).

Here we test the newest generation of high-resolution satellite DEMs (5 m AW3D5 and 10 m TSX/TDX) for assessing the hillslope-to-valley transition measured by L_H as well as differences in relief, slope angles, and curvature upstream and downstream of the knickpoint in the 66 km^2 Quebrada Honda catchment (Fig. 2). We compared results from this analysis with the 30 m SRTM-C for its high quality and widespread use. In addition, we analyzed the AW3D5 bilinearly resampled to 10 and 30 m to examine differences in resolution independent from sensor biases (Grieve et al., 2016c). We did not include the ASTER DEMs in hillslope analyses because of elevation noise prevalent in these 30 m DEMs. We also excluded the 30 m AW3D30 as linear step-like artifacts on hillslopes, likely caused by the resampling technique of the

Japanese Aerospace Exploration Agency (JAXA), obfuscates slope and curvature calculations. We combined measures of curvature and slope distributions with slope-area, slope-curvature, and curvature-area plots to demonstrate differences in morphology in the upstream and downstream catchments. In a second step, we explored sub-basin convex curvature (from the 5 m DEM) and slope (from the 5-30 m DEMs) in relation to knickpoint location in search of transient hillslope morphology signals.

For each DEM, we calculated mean and SD of relief upstream and downstream of the knickpoint in a 1 km moving window. Since hillslopes represent a diffusive environment where flow is multi-directional, we calculated drainage area and slope using the D∞ algorithm (Tarboton, 2005). Curvature was calculated using the Laplacian of elevation (e.g., Tarolli and Dalla Fontana, 2009):

$$C = \nabla^2 z = \left(\frac{\delta^2 z}{\delta x^2} + \frac{\delta^2 z}{\delta y^2} \right) \tag{4}$$

where concavity (valleys and channels) is denoted by $C > 0$, convexity (hillslopes and ridges) is denoted by $C < 0$, and planar slopes are denoted by $C = 0$ (Fig. 2D). Wiener filtering (Wiener, 1949) in a nine-pixel window was carried out prior to curvature calculations during initial tests. Although this smoothing technique emphasized sharp ridges and narrow valleys for some DEMs, it was found to reduce the curvature variability captured in the 5 m data (cf. Appendix D, Figure D1). Thus, for further calculations, raw curvature from the unfiltered DEM was preferred. Distributions of slope and curvature (all curvature and convex curvature alone) were visualized as box plots displaying medians, 25-75th percentile ranges, 1st and 99th percentile cutoffs, and all outlier measurements.

We generated plots of mean slope and mean curvature ± 1-σ versus logarithmically binned contributing area and plots of mean slope ± 1-σ versus linearly binned curvature (all separated upstream and downstream of the knickpoint). For slope-area plots, the gradient at the graphical rollover in binned area is recorded along with this area bin. By dividing this area bin by the DEM resolution, we acquire a measurement for horizontal L_H (e.g., Roering et al., 2007; Grieve et al., 2016a). We also used 2-D kernel density estimates (Botev

et al., 2010) to identify the densest concentrations of slope and area values, but found similar results to the graphical approach. As an additional comparison, we used the curvature-area and slope-curvature plots to visualize the slope and area trends related to curvature, particularly around the zero curvature planar inflection point in the landscape (Roering et al., 1999).

Following assessment of upstream and downstream (and inter-DEM) differences in slope, curvature, hillslope length, and relief, we focused on sub-basin variability related to the knickpoint in the Quebrada Honda. Here, we manually selected basin pour points to insure sampling of large enough basins with internal hilltops and valleys for averaging hillslope signals. A total of 27 basins were selected for this analysis with seven fully downstream of the knickpoint, two near the knickpoint lip, and the remaining basins upstream of the over-steepened channel reach. Minimum sub-basin area was 0.25 km^2, maximum area was 6.9 km^2, and the mean area was 1.8 km^2. In an attempt to isolate hilltop pixels from the 5 m AW3D5 DEM to assess patterns of erosion related to the knickpoint (Hurst et al., 2012), convex curvature was extracted from each sub-basin and filtered to remove any pixels with drainage areas of > 100 m^2, slopes > 0.8 m/m, and finally any isolated patches of < 20 pixels. Slopes and filtered convex curvatures for each sub-basin were plotted as mean $\pm$ 1-σ and box plots showing the full distribution around the median. Mean- and median-centered results were plotted as the sub-basin's relative distance upstream of the Quebrada Honda outlet, alongside a map view of sub-basin location and channel steepness (k_{sn}) for all channels with > 0.1 km^2 drainage area.

4. Results

4.1. Elevation Accuracy

Vertical uncertainties, measured as the mean ± SD of differences between DEM elevation and rasterized dGPS height, for all DEMs are summarized in Table 2.

Table 2. Results of pixel-by-pixel DEM vertical accuracy (DEM minus dGPS).

Dataset	Mean of dGPS uncertainty (m)	SD of dGPS uncertainty (m)	Number of rasterized measurements[a]	Reduction by ±30 m outlier filtering (%)
30 m SRTM-C	2.81	3.33	64,782	0.02
30 m AW3D30	1.59	2.81	63,413	0.03
30 m ASTER GDEM2	-0.86	9.48	63,308	2.30
30 m ASTER Stack[b]	4.56	6.93[c]	15,506	0.12
10 m TSX/TDX (February 7, 2011)	1.99	2.02	28,982	0.03
10 m TSX/TDX (November 6, 2012)[d]	1.32	3.83	22,182	0.00
10 m TSX/TDX (August 25, 2013)	2.94	3.22	22,175	0.00
5 m AW3D5	2.40	1.64	14,306	0.00

a, After ±30 m outlier filtering
b, Generated for Pocitos Basin by weighted stacking of eight manually generated ASTER L1A DEMs
c, Compare with 11.42 m and 10.06 m SD for single L1A DEM and ASTER GDEM2, respectively
d, DEM selected for geomorphometric analysis

For visual comparison, the vertical uncertainty distributions are plotted for the 30 m (Fig. 3) and higher resolution (Fig. 4) DEMs. Despite its low SD, visual inspection of step-like artifacts on some hillslopes, likely caused by resampling at JAXA, revealed the inadequacy of the AW3D30 for assessing geomorphic metrics. The low SD and smooth appearance of the SRTM-C led to our selection of this 30 m DEM for further analysis. The improvement in quality through weighted stacking of ASTER L1A stereopair DEMs is apparent in the reduction of the SD from 11.42 m for a single L1A DEM to 6.93 m for the Stack, although all ASTER DEMs extend well beyond the ±30 m outlier cutoff (Figure 3B).
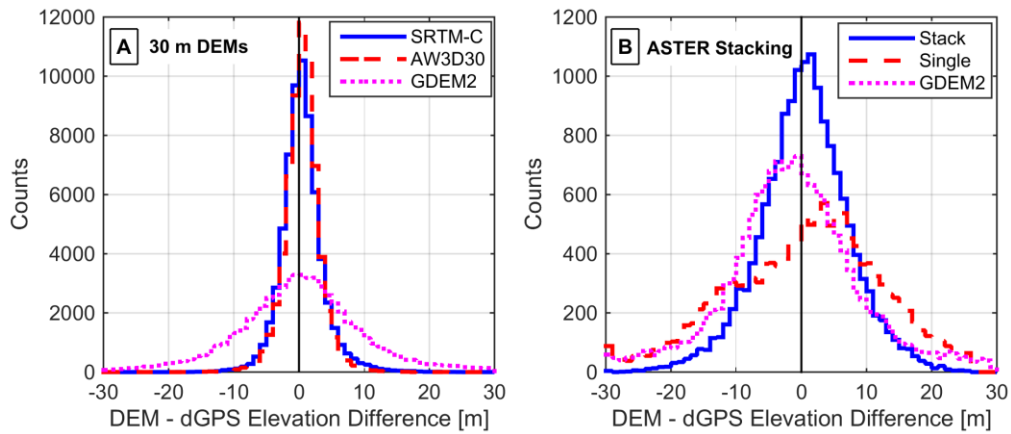
Figure 3. (A) Global 30 m DEM vertical uncertainty measured as difference between DEM elevation and rasterized dGPS measurement. (B) ASTER 30 m DEM vertical uncertainties from the Pocitos Basin. Plots have been normalized by mean offsets. Mean, SD, count, and percent reduction in outliers reported in Table 2. Note the order of magnitude difference in scale, as (B) is centered only on the Pocitos Basin (~2,500 km^2), whereas (A) spans all dGPS measurements (~55,000 km^2) (Fig. 1A).

For the higher resolution DEMs (Fig. 4), we note the narrow uncertainty distributions having no ±30 m outliers, with the exception of a small number (0.03 % reduction) for the February 7, 2011 TSX/TDX DEM centered on the Salar de Pocitos. The 5 m AW3D5 has the lowest uncertainty of any DEM (Table 2), indicating its superiority, even in the steep terrain around the Nevado Queva (Fig. 1B), for which a dGPS track exists. The wider, double peaked uncertainty distributions for the November 6, 2012 and August 25, 2013 TSX/TDX DEMs are caused by their coverage over variable terrain east of the Salar de Pocitos, where accurate DEM generation is complicated by radar shadowing and layover in steeper topography. Visual inspection of these two DEMs containing the full Quebrada Honda catchment revealed hillslope artifacts on both, however, the 2013 DEM had noticeable staircase-like contours, whereas the 2012 DEM had a smoother appearance. Therefore, the 10 m TSX/TDX DEM from November 6, 2012 was selected for further geomorphic comparison. A few minor artifacts on hillslopes in the Quebrada Honda were edited by edge interpolation, whereby a distance-weighted value was taken from the borders of a polygon manually generated around the artifact and used to fill new values in the polygon area, resulting in smoother representation of the landscape.
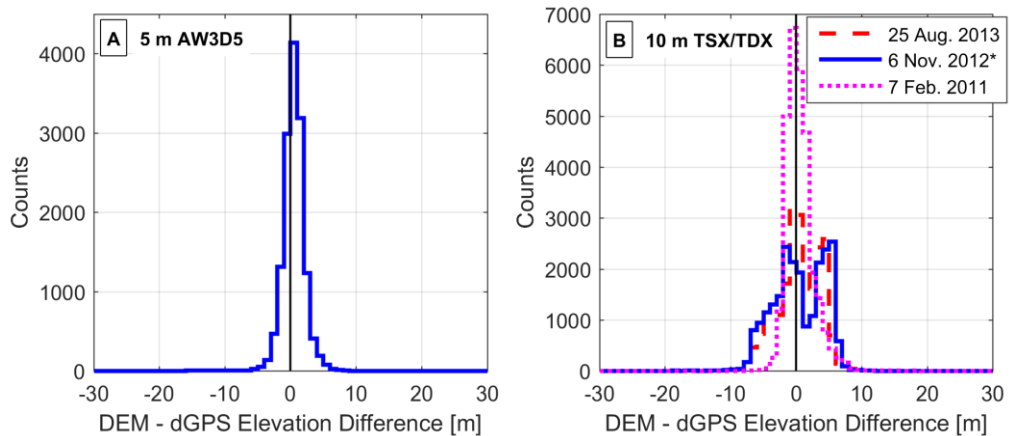
22

Figure 4. (A) 5 m AW3D5 vertical uncertainty measured as difference between DEM elevation and rasterized dGPS measurement. (B) 10 m TSX/TDX vertical uncertainties. Plots have been normalized by mean offsets. Mean, SD, count, and percent reduction in outliers reported in Table 2. AW3D5 clip covers the Quebrada Honda and steep terrain on the Nevado Queva (Fig. 1B). The TSX/TDX DEM from February 7, 2011 covers the flat Salar de Pocitos, whereas the two DEMs from 2012 and 2013 cover more mountainous terrain east of the salar (with coverage over the Quebrada Honda), leading to greater uncertainties in elevation measurements. The star (*) denotes the 2012 TSX/TDX DEM selected for geomorphometric analysis

In addition to vertical SD, we examined the distribution of vertical uncertainty with respect to elevation, slope, and aspect of the topography for the 30 m global DEMs. Results for the SRTM-C, ASTER GDEM2, and AW3D30 are presented as binned box plots in Figures 5-7. Uncertainties for each bin are plotted without filtering ±30 m outliers. We note the narrow uncertainty range for the SRTM-C and AW3D30 compared to the ASTER GDEM2. Furthermore, the ASTER GDEM2 appears to have a slight aspect related bias with an amplitude of only ~5 m (Fig. 6C). On each plot we note the dearth of dGPS measurements on slopes above 30°, as the majority of measurements were taken from low gradient roads and flat salars.
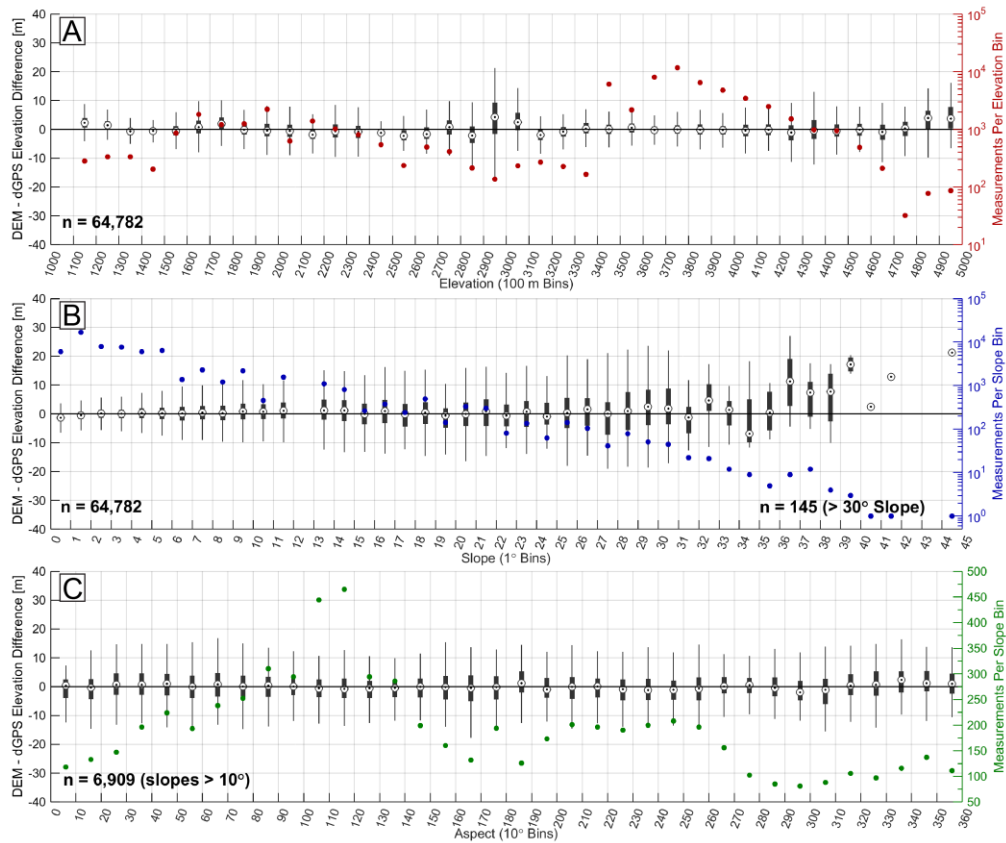
Figure 5. SRTM-C (A) elevation, (B) slope, and (C) aspect vertical uncertainty bias. Median elevation difference (black unfilled circles) with 25-75th percentile range (boxes) and 1st and 99th percentile outlier cutoff (whiskers) plotted for each bin on left axis. Number of measurements indicated (n) with measurements per bin plotted as colored circles on right axis. For aspect (C), only measurements on slopes > 10° are used. Elevation differences are normalized by mean offset. We note the dearth of slope measurements > 30° (B).
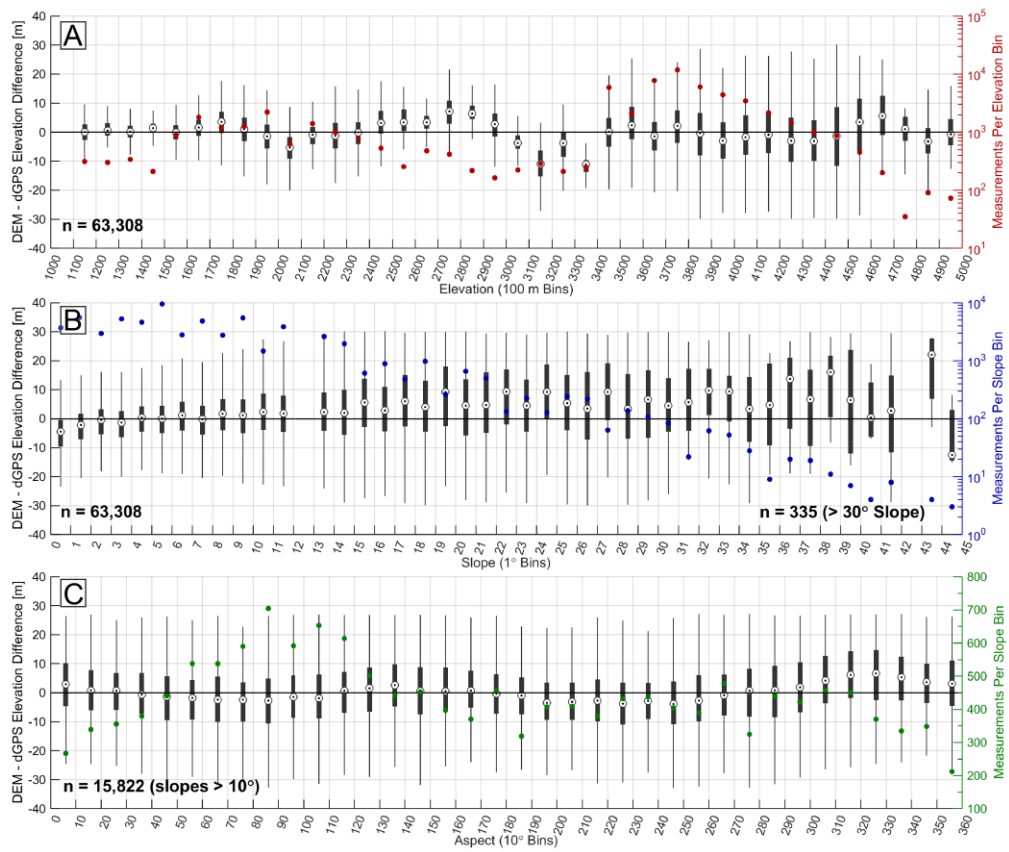
Figure 6. ASTER GDEM2 elevation (A), slope (B), and aspect (C) vertical uncertainty bias. Note the wide uncertainty range (bars and whiskers) extending to the full axis scale.
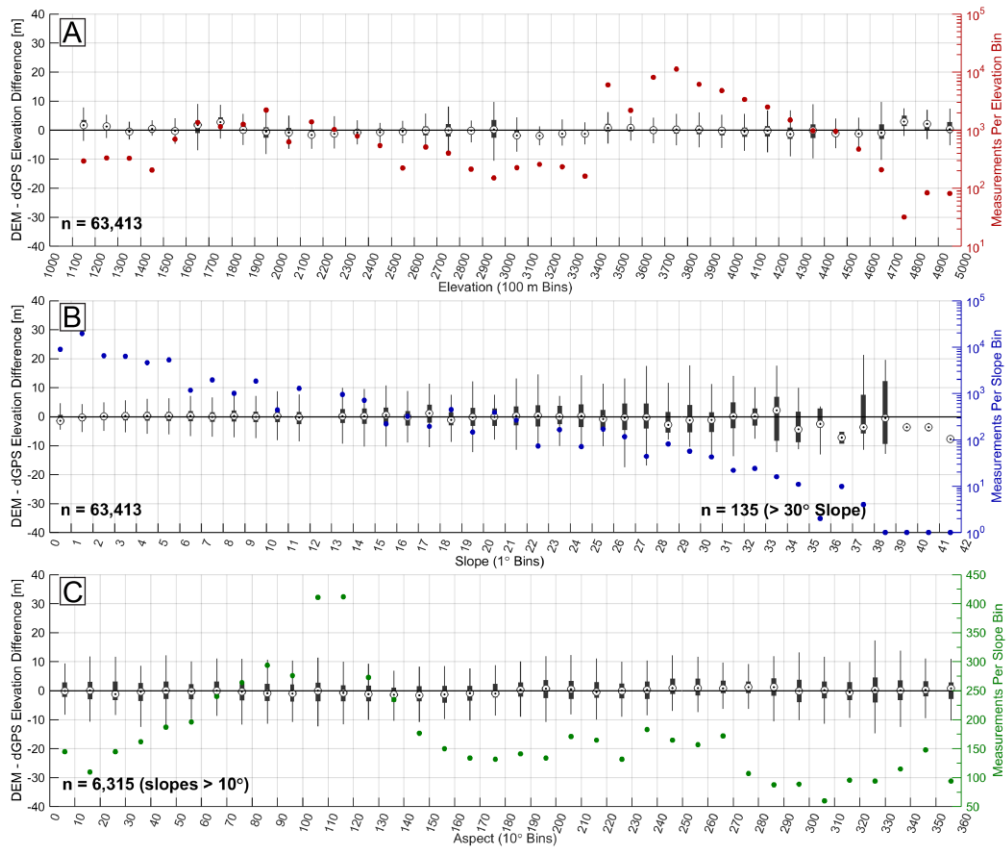
Figure 7. AW3D30 elevation (A), slope (B), and aspect (C) vertical uncertainty bias. Note the narrower range of uncertainty (bars and whiskers) compared to Figure 5 (SRTM-C) and Figure 6 (ASTER GDEM2).

4.2. Geomorphometric Analysis

Based on the results of elevation validation and visual inspection of the datasets, we selected the 30 m SRTM-C, the 10 m TSX/TDX (from November 6, 2012), and the 5 m AW3D5 for assessing geomorphic metrics in the Quebrada Honda catchment.

4.2.1. Channel Profile Analysis

The results of m/n estimation from least-squares R^2 maximization (Perron and Royden, 2013; Schwanghart and Scherler, 2014) and from piece-wise fitting (Mudd et al., 2014) on the Quebrada Honda trunk channel are summarized in Table 3. Both methods provide similar estimates of m/n for the trunk channel, falling in a range of 0.51-0.57. While the least-squares technique takes only a few minutes to setup and run, the computationally intensive piece-wise fitting technique takes hours to days, although provides a range of minimum $AICc$ that denote plausible m/n values.

Table 3. m/n values using two chi plot methods on Quebrada Honda trunk.

Dataset	SD of dGPS uncertainty (m)	Least-squares[a]		Piece-wise Fitting[b]		
		m/n	R^2	$AICc$ minimum value $\pm$ SD	m/n at $AICc$ minimum	Plausible values of m/n[c]
30 m SRTM-C	3.33	0.52	0.97	27.98 ± 0.50	0.55	0.55-0.57
10 m TSX/TDX	3.83	0.56	0.97	28.89 ± 0.22	0.54	-[d]
5 m AW3D5	1.64	0.51	0.98	31.54 ± 0.21	0.54	0.53-0.56

a, Peron and Royden (2013) and Schwanghart and Scherler (2014)
b, Mudd et al. (2014)
c, With corresponding $AICc$ value falling within SD range of $AICc$ minimum
d, No tested values of m/n fell within the $AICc$ SD range

4.2.2. Hillslope Analysis

Relief values in a 1 km window varied little between DEM, confirming results of previous studies which showed that relief depends only on the spacing of ridges and valleys being at least twice the resolution of the DEM (e.g., Grieve et al., 2016c), which for our study is at least 60 m. Downstream of the knickpoint, 1 km relief for all DEMs was approximately 525 m with SD = 150 m, whereas upstream relief was lower at 340 m and less variable with SD = 110 m. Box plots separated upstream and downstream the knickpoint showing distributions for slope, all curvature, and convex curvature alone are presented in Figure 8.
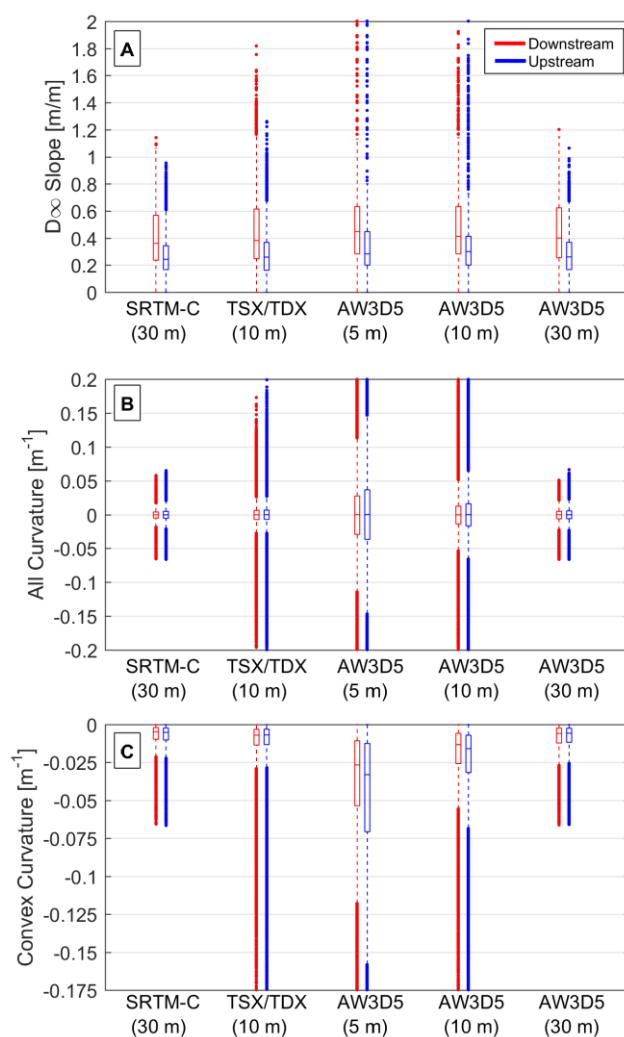

Figure 8. Slope (A), all curvature (B), and convex curvature (C) box plots separated upstream (blue) and downstream (red) for the three 5-30 m DEMs and for the 5 m AW3D5 resampled to 10 and 30 m. Center line is median, boxes are 25-75th percentile range, dashed whiskers extend to 1st and 99th percentiles, and all outliers are plotted as points.

From Figure 8A, we note that median slopes downstream of the knickpoint are consistently 0.1-0.2 m/m greater in magnitude than upstream, regardless of DEM resolution. Furthermore, the quartile and outlier range (denoted by the box and whiskers, respectively) is very similar regardless of DEM resolution, with only the outlier points growing in number and spread with decreasing resolution, demonstrating the greater variability (more outliers) measured on the higher resolution AW3D5 5 m DEM. Resampling of this DEM to 10 m also displays more outliers compared with the 10 m TSX/TDX, however, at 30 m resampling the distribution becomes very similar to the 30 m SRTM-C DEM. Importantly, we note that although slope values (besides outliers) are similar between all DEMs, the curvature distributions vary significantly. Both the 10 m TSX/TDX and 30 m SRTM-C have very narrow quartile and outlier ranges compared with the wide distribution of the 5 m AW3D5 (Fig. 8B-C). However, the 10 m TSX/TDX measures far more outliers compared to the 30 m SRTM-C, whose full distribution extends only to approximately ± 0.05 m^{-1} (Fig. 8B). Similar to slope results, the AW3D5 resampled to 10 m has a wider distribution than the TSX/TDX at the same resolution, however, the distribution of the AW3D5 30 m (resampled) resembles the 30 m SRTM-C distribution. Compared to upstream, the downstream curvatures have a slightly narrower range as indicated in the 5 m data (Fig. 8B-C). When examining convex (negative) curvature alone we note the upstream median and range plot slightly more negatively (more convex) than downstream, although more convex curvature outliers are found downstream (Fig. 8C).

Slope-area, curvature-area and slope-curvature plots separated at the knickpoint are presented in Figures 9-11. The higher slopes downstream of the knickpoint (Fig. 8A) are reflected in binned averages with typically 0.1-0.2 m/m greater magnitude downstream given the same contributing area, regardless of DEM resolution. Moving from 30 to 10 to 5 m resolution, the values for average local slope (and slope at the rollover) increase slightly, indicating the higher slope values measured from higher resolution DEMs. Also, the critical drainage area demarcating the approximate hillslope-to-valley transition (and thus hillslope length) identified at the rollover in slope value also decreases with increasing resolution. For the 10 and 30 m DEMs L_H is 30-40 m less upstream

of the knickpoint, whereas for the 5 m DEM the L_H value is identical upstream and downstream. Upstream critical drainage area values are 4,440 m², 890 m², and 280 m², and downstream values are 5,580 m², 1,170 m², and 280 m² for the 30, 10, and 5 m DEMs, respectively. The large scatter in averaged slope values prior to the rollover in drainage area (i.e., in the hillslope realm) for the 5 m AW3D5 DEM may be partially caused by fine-scale diffusive hillslope processes, however, we note that this dataset was received in an integer rather than floating point format, which lead to discontinuous slope calculations from the D∞ algorithm, because of limited elevation values.
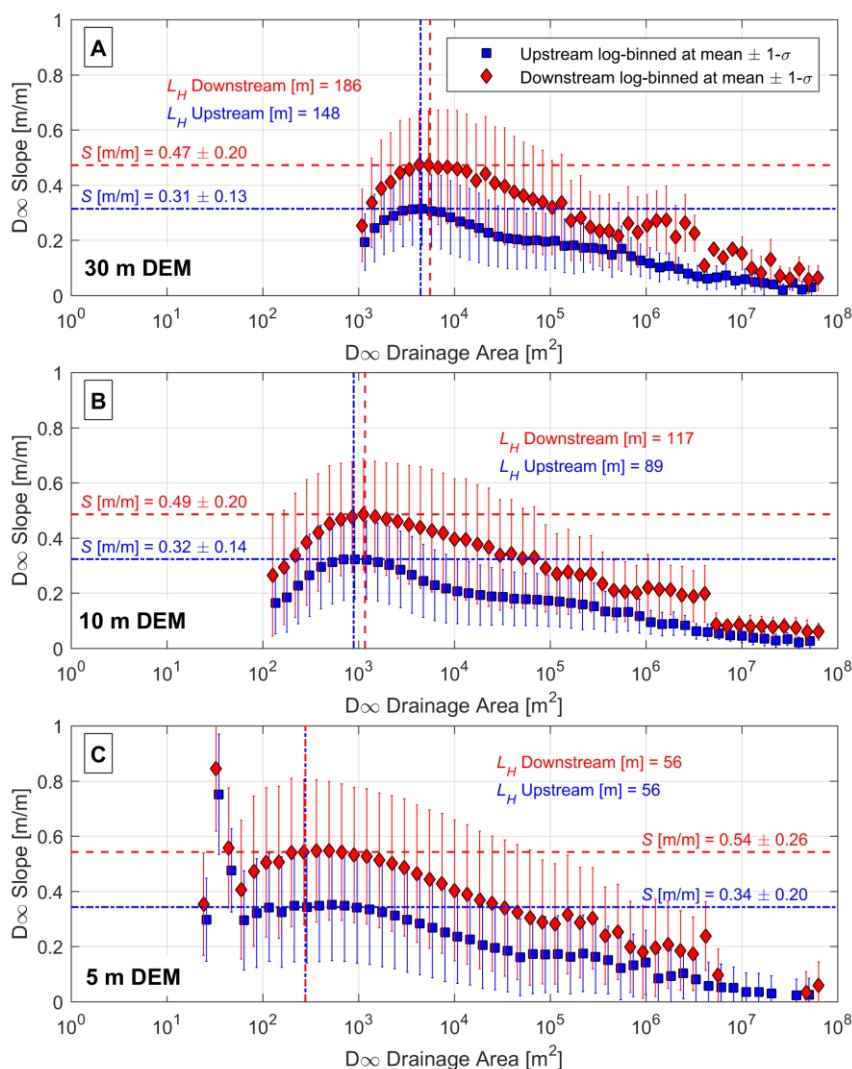

Figure 9. Slope binned by logarithmic area at the mean with standard deviations indicated for SRTM-C 30 m (A), TSX/TDX 10 m (B), and AW3D5 5 m (C) DEMs. Analysis separated downstream (red diamonds) and upstream (blue squares) of the knickpoint. Horizontal L_H measured by dividing critical drainage area (horizontal line) by DEM resolution, with slope value at this bin noted.

The greater curvature variability captured in the 5 m data is again demonstrated in curvature-area plots, with greater standard error bars around the mean (Fig. 10C). While little difference is noticeable upstream or downstream in the 10 and 30 m DEMs, we note that downstream area bins have slightly lower concave curvatures (more planar) than the corresponding upstream area bins in the 5 m data. For all three DEMs, there appears to be a scaling break at the zero curvature planar inflection point.
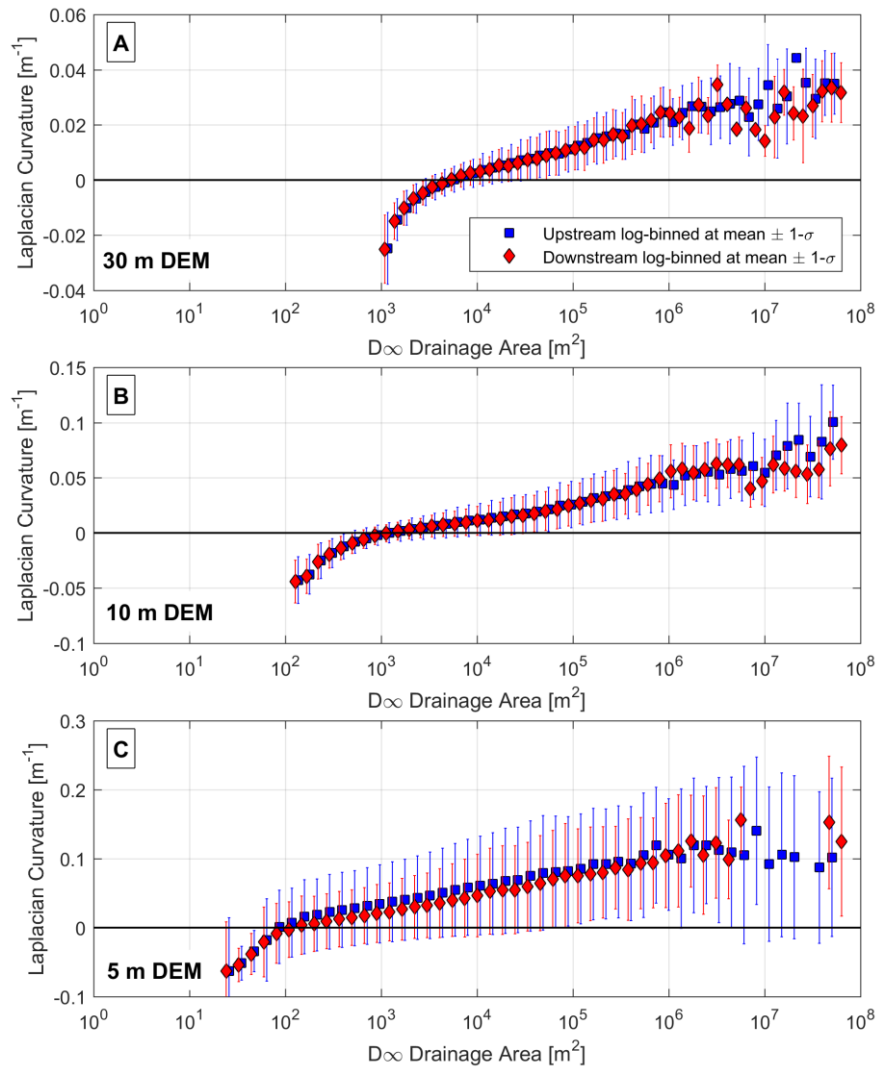

Figure 10. Curvature binned by logarithmic area at the mean with standard deviations indicated for SRTM-C 30 m (A), TSX/TDX 10 m (B), and AW3D5 5 m (C) DEMs. Analysis separated downstream (red diamonds) and upstream (blue squares) of the knickpoint. Greater variability in curvature (larger error bars and greater y-axis range) is measured in the 5 m data.

Figure 11 demonstrates the relationship between slope and curvature upstream and downstream of the knickpoint, again indicating greater curvatures (wider x-axes) and similar slopes (same y-axes and error bar lengths) measured from 30 to 10 to 5 m resolution. From this, we note that slopes at high convex (negative) and concave (positive) curvatures are similar upstream and downstream, with greater differences on more planar slopes. The scatter of slopes at high convex curvatures in the AW3D5 5 m data likely indicates the fine-scale hillslope processes captured by this dataset, though are again influenced by the integer data format.

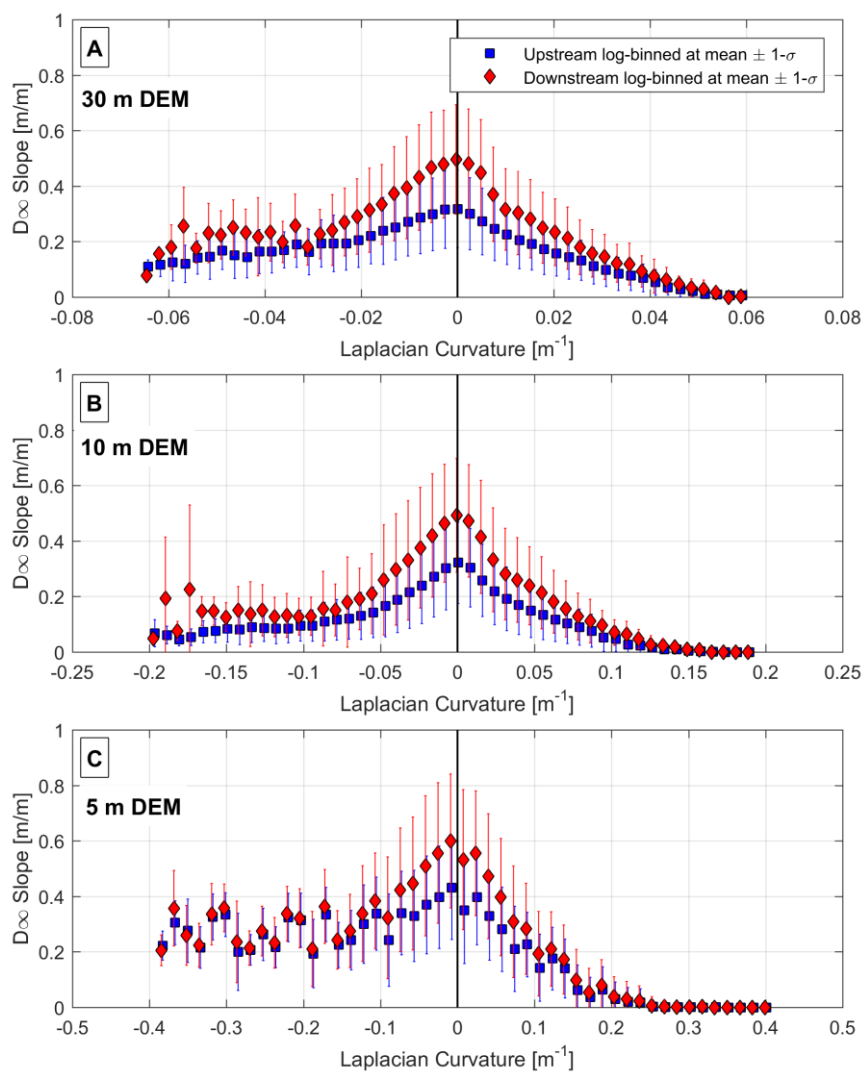Figure 11. Slope binned by curvature at the mean with standard deviations indicated for SRTM-C 30 m (A), TSX/TDX 10 m (B), and AW3D5 5 m (C) DEMs. Analysis separated downstream (red diamonds) and upstream (blue squares) of the knickpoint. Greater variability in curvature is measured in the 5 m data, especially in the convex (negative) curvatures. Note the growing y-axis with increasing resolution.

Based on the wide AW3D5 5 m curvature distribution and the differences in slope upstream and downstream of the knickpoint, we sought to assess intra-catchment variability of sub-basins upstream and downstream of the knickpoint with respect to their relative distance from this dynamic feature. Figures 12 and 13 demonstrate this analysis on the 5 m AW3D5 dataset. These plots were generated by taking the mean and standard deviation of the ridge-crest filtered convex curvatures (filtering detailed in methods) and full slope distributions for each of the 27 basins. From Figure 12, we note no discernable trend in convex curvature related to the knickpoint with uncertainties overlapping for each DEM. Box plots of these distributions also show large overlap and no apparent trend (Appendix E, Fig. E1). On the other hand, for slopes (Figure 13) we see a slight trend of higher slopes downstream of the knickpoint, a peak in slope at basin 8 just downstream of the knickpoint, and then decreasing (although highly variable) slopes to the upper catchments (basins 24-27). Box plots of these slope distributions do not show this trend as clearly as they are influenced by the limited slope values calculated on this integer format DEM, resulting in many identical median values (Appendix E, Fig. E2).

Figure 12. AW3D5 5 m mean and standard deviation of filtered convex curvature (A) plotted for manually selected sub-basins (B). Channel steepness indicates approximate knickpoint lip location between basins 8 and 9. Number of measurements in each basin indicated by colored circles plotted at the mean value in (A). Curvature calculated as Laplacian of elevation [equation (4)] on unfiltered DEM (cf. Appendix D, Figure D1A). All channels with drainage area > 0.1 km² plotted in (B).
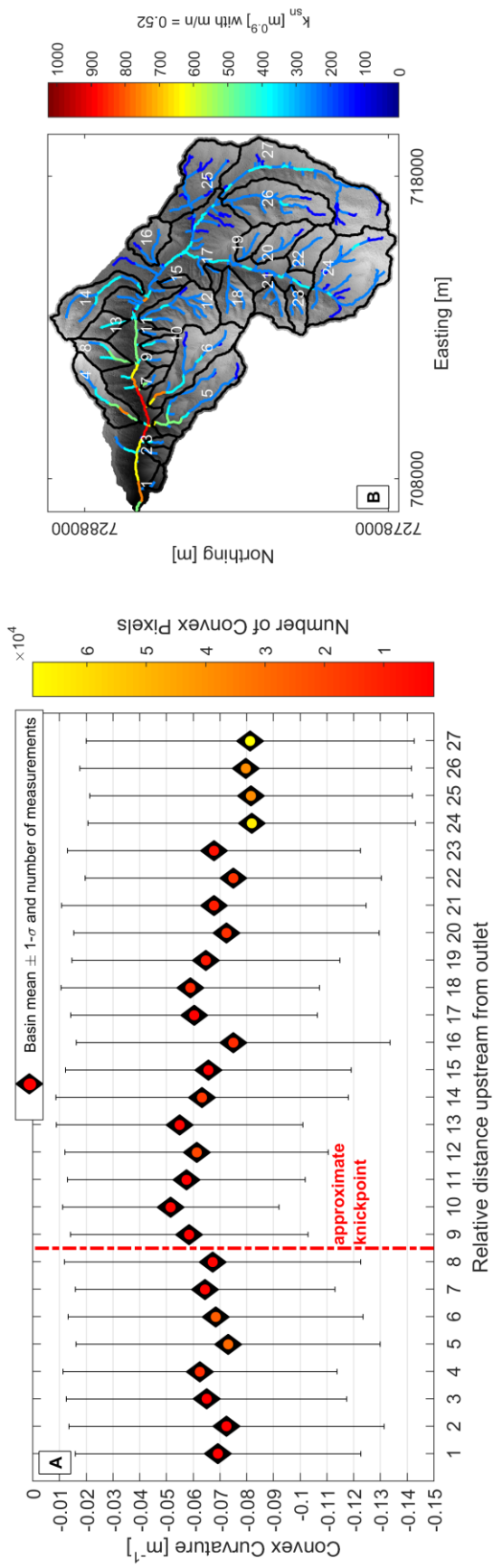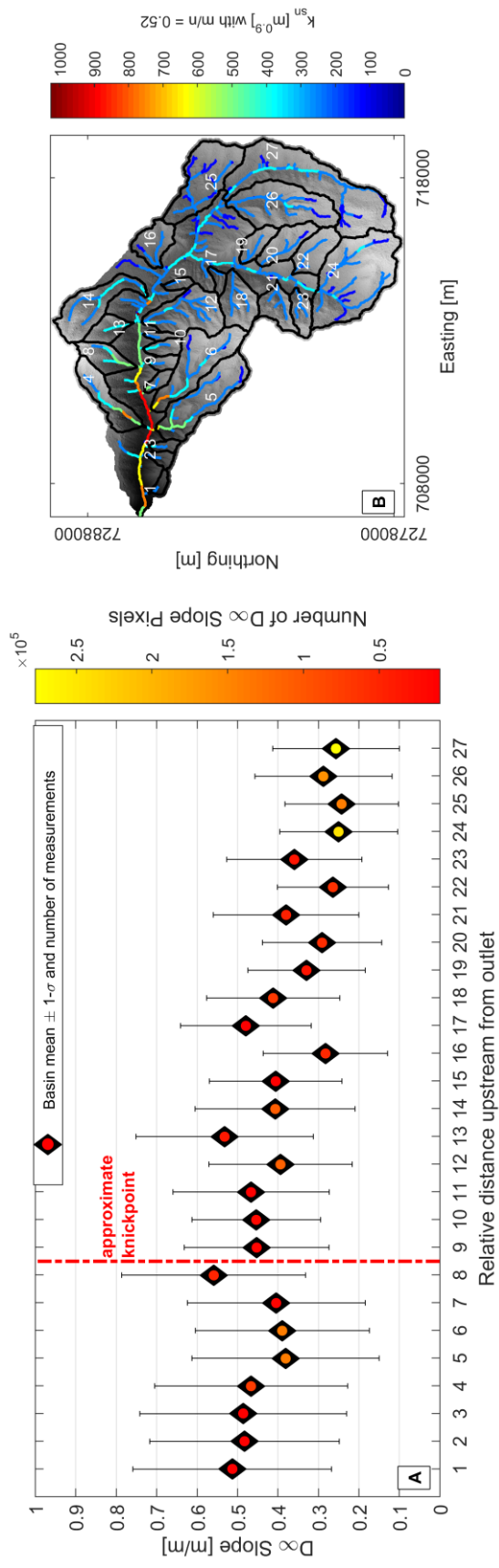
Figure 13. AW3D5 5 m mean and standard deviation of slopes (A) plotted for manually selected sub-basins (B). Channel steepness indicates approximate knickpoint lip location between basins 8 and 9. Number of measurements in each basin indicated by colored circles plotted at the mean value in (A). All channels with drainage area > 0.1 km² plotted in (B).

5. Discussion

5.1. Elevation Validation

5.1.1. 30 m DEMs

The low quality of the ASTER GDEM2 is apparent in the wide uncertainty distribution (Fig. 3A). The uncertainties for this DEM extend beyond the ±30 m outlier cutoff, leading to a > 2 % reduction in total measurements used to assess uncertainty, but a SD remaining near 10 m (Table 2). For over 228,000 Australian National Gravity Database station heights with < 1 m vertical accuracy, Rexer and Hirt (2014) found similar results for the GDEM2 with SD ranging from 7.7 m in flat terrain to 11.29 m in mountainous regions. Other studies have reported vertical accuracies of 3-6 m for the GDEM2, but these are often determined with fewer (10s to 100s) high accuracy control points compared with our study using over 300,000 dGPS measurements (e.g., Mukherjee et al., 2013; Athmania and Achour, 2014; Bagnardi et al., 2016). Our results indicate that in a mountainous, non-vegetated region the GDEM2 falls short of the reported vertical accuracy of 8.86 m (Tachikawa et al., 2011), even when ignoring gross outliers. Uncertainty was improved in the ASTER Stack generated for the Pocitos Basin to SD of 6.93 m with only 0.12 % outlier reduction, versus 10.06 m and 3.89 % outlier reduction for the GDEM2 clipped to the same area (Fig. 3B). This Stack represents an improvement over individual ASTER L1A stereopair DEMs with reported accuracies of 7-60 m (e.g., Toutin and Cheng, 2001; Hirano et al., 2003; Kääb, 2005; Nuth and Kääb, 2011). Despite this, the ASTER Stack was deemed insufficient for geomorphometry after visual inspection revealed remaining noise on hillslopes and channel elevation profiles, complicating accurate slope and curvature measurements.

In addition to the largest vertical uncertainty, the ASTER GDEM2 displays the largest uncertainties with respect to each topographic characteristic (elevation, slope, and aspect) as indicated by large quartile bars and outlier whiskers for each bin, extending to almost ±40 m (Fig. 6). An increase in uncertainty is apparent with increasing slopes, indicating over prediction of elevation for the ASTER GDEM2 at higher slopes, however, we also note the

decrease in number of measurements at higher slopes (Fig. 6B). The GDEM2 experiences a clear aspect bias with an amplitude of ~5 m repeating at ~65°, ~135°, ~195°, and ~325° (approximately ENE, SE, WSW, and NNW) (Fig. SM2C), which is lower than the ~50 m aspect bias reported in far-north glaciated terrain (Nuth and Kääb, 2011).

Both the SRTM-C and AW3D30 have narrow distributions with a SD of 3.33 and 2.18 m, respectively, and less than 0.04 % reduction in measurements from ±30 m outlier removal (Table 2). While elevation accuracy has not been previously reported for the AW3D30, our results indicate that this dataset meets mission specifications of < 5 m vertical accuracy (Tadono et al., 2014). Most elevation accuracy reporting for the SRTM DEMs have centered on the 30 m X-band and 90 m C-band products (e.g., Rexer and Hirt, 2014; Mukherjee et al., 2013; Kolecka and Kozak, 2014), and not the 2014 globally-released (previously only USA) 30 m C-band DEM used here. Our SRTM-C results are in close agreement with the 3.64 m accuracy found using 19 high accuracy ground measurements for a steep volcano (Bagnardi et al., 2016) and less than the 8 m accuracy versus a control DEM on another volcano in Hawaii (Kervyn et al., 2008). Hofton et al. (2006) report a vertical SD of 2-7 m for low vegetation regions in the USA for the SRTM-C versus high accuracy lidar data. For the 30 m SRTM-C our results exceed the 6.2 m vertical accuracy found by Rodriguez et al. (2006) for dGPS tracks across South America.

The SRTM-C (Fig. 5) and AW3D30 (Fig. 7) exhibit no apparent biases with respect to elevation or aspect. Both DEMs show smaller ranges of uncertainties than the ASTER GDEM2 (shorter boxes and whiskers). This is especially pronounced in the AW3D30 with the narrowest uncertainty ranges plotted. The SRTM-C does exhibit a somewhat greater uncertainty at higher slopes (Fig. 5B), but there are few measurements at theses high slopes to confirm this. The uncertainties at higher slopes for the SRTM-C show overestimation of elevation, in agreement with the findings of Shortridge and Messina (2011). On the other hand, the AW3D30 indicates lower uncertainties (but still increasing) at these higher slopes (Fig. 7B). Previous studies suggesting SRTM-C biases related to slope and aspect (e.g., Berthier et al., 2006; Berthier et al., 2007; Van Niel et al., 2008; Shortridge and Messina, 2011) cannot be discounted by our

findings, however, we expect lower uncertainties with respect to slope in our non-glaciated, vegetation-free study area, where effects like radar penetration (e.g., Rignot et al., 2001; Becek, 2008; Gardelle et al., 2012) are minimal. Radar associated biases are not present in the AW3D30 as this DEM was generated through optical methods by stacking of ALOS PRISM tri-stereopairs (Panchromatic Remote-sensing Instrument for Stereo Mapping, see Appendix B for details).

Results of 30 m global DEM elevation validation indicate the high quality of both the SRTM-C and AW3D30 compared to the ASTER GDEM2. The ASTER GDEM2 is a far noisier dataset, which complicates geomorphic analyses requiring accurate slope and curvature calculations (e.g., Kervyn et al., 2008; Fisher et al., 2013). This noise is persistent, although slightly reduced, in the manually generated ASTER Stack (Fig. 3B). The AW3D30 performed best in terms of agreement with dGPS measurements and limited biases with respect to elevation, slope, and aspect (Fig. 7). However, the SRTM-C also performed comparably well. Since the SRTM-C accuracy has been more widely reviewed in the literature and the AW3D30 has many large no-data voids (which may be reconciled in future releases) and clear step-like artifacts (likely caused by resampling at JAXA), we chose the SRTM-C as our 30 m comparison dataset for geomorphometry.

5.1.2. 5-10 m DEMs

For the high resolution regional DEMs, our results indicate the higher quality (lower uncertainty) of the commercial AW3D5 optical DEM compared to the interferometrically generated TSX/TDX radar DEMs, with lower values for SD (Table 2; Fig. 4). Similar to the AW3D30, the vertical uncertainty for the AW3D5 exceeds the mission standard of < 5 m (Tadono et al., 2014). The low SD of 2.02, 3.83, and 3.22 m for our three TSX/TDX DEMs are in close agreement with reported vertical accuracies of 5.74 m versus ground control points (Bagnardi et al., 2016), 3.57 m versus lidar data (Du et al., 2015), and < 2 m versus laser altimetry (Rossi et al., 2016) for interferometrically generated TSX/TDX DEMs with resolutions of 5-12 m. Wider, bimodal uncertainty

distributions for the TSX/TDX DEMs covering the Quebrada Honda and Nevado Queva (2012 and 2013 DEMs in Figure 4B) are likely related to radar shadowing and layover in steeper terrain. As these TSX/TDX DEMs were generated from single pass radar scenes, we expect some improvement with stacking of many scenes, however, this improvement was not found by stacking the two TSX/TDX DEMs generated here. As the TSX/TDX radar pairs were also used to generate the commercial WorldDEM 12 m product, we expect slightly lower quality of the WorldDEM compared to the AW3D5 in our study region, but this requires verification. This is especially relevant given the higher costs (and lower resolution) of the WorldDEM (although the AW3D5 contains many no-data voids).

Elevation accuracy for both the higher resolution DEMs is similar to the high quality public global DEMs (SRTM-C and AW3D30). The close agreement in vertical uncertainty (all < 3.5 m) between the 5-30 m datasets necessitates our geomorphic metric comparisons. Our data shows that accurate elevation data are negligibly influenced by grid size at these resolutions (Vaze et al., 2010), making differences in DEM quality for deriving geomorphic metrics unapparent from the pixel-by-pixel comparison and SD metric.

5.2. Geomorphometric Validation

5.2.1. Channel Profiles

We note that the m/n values for the Quebrada Honda trunk correspond surprisingly well across the datasets and between the chi plot methods (Table 3). This is despite the fact that the knickpoint causes the channel to plot non-linearly in chi space using the least-squares method, whereas the piece-wise method allows exact fitting (Appendix C, Fig. C1 and C2). These values (0.51-0.57) fall well within the range of reported m/n values in a variety of other settings (e.g., Wobus et al., 2006; Kirby and Whipple, 2012). Testing on the 30 m DEMs revealed similar m/n values regardless of the elevation noise. For instance, the ASTER GDEM2, which had the largest vertical uncertainty and noisiest appearance, returned $m/n = 0.52$ with $R^2 = 0.97$ using the least-squares method, which is identical to the SRTM-C results. The only difference for the

higher resolution datasets is a slightly lower SD (uncertainty) of minimum *AICc* for piece-wise fitting: ~0.5 for the 30 m versus ~0.2 for the 5 and 10 m DEMs. On the other hand, the R^2 values from least-squares fitting are nearly identical for all three DEMs. Differences in *m/n* values between the datasets are likely caused by differences in channel lengths, whereby the higher resolution DEMs are able to better resolve the channel location. The *m/n* values calculated using either chi plot method are comparable regardless of DEM resolution (or noise, as indicated by the ASTER GDEM2 results). This result only holds for relatively simple channel shapes, like the Quebrada Honda, whereas the inclusion of tributaries and more complex settings may warrant further testing and the preferred use of the statistically robust piece-wise fitting method (Mudd et al., 2014). Consideration of different channel lengths and changes in *m/n* may be an important factor when using the ASTER GDEM2 for chi plot analysis as this dataset has demonstrated excessive channel foreshortening over long stretches (Fisher et al., 2013).

5.2.2. Hillslopes

Examination of the hillslope-to-valley transition denoted by the characteristic transport length using slope-area plotting (horizontal L_H), along with the calculation of relief, slope, and curvature provide an additional check on DEM quality and applicability to analyses that have become increasingly restricted to lidar (e.g., Roering et al., 2007; Roering et al., 2013; Hurst et al., 2012; Tarolli, 2014; Passalacqua et al., 2015; Grieve et al., 2016a, b, c; Clubb et al., 2016).

Slope measurements are broadly similar between DEMs, although we note that more extreme slopes are only captured in the higher resolution data (Fig. 8A). The superiority of the 5 m AW3D5 data for capturing curvature variability in the landscape is apparent in the wider distributions measured for this geomorphic metric. This is further confirmed by the wider distributions found when resampling this data to 10 m in comparison to the 10 m TSX/TDX DEM. Interestingly, when resampling to 30 m resolution, the AW3D5 data loses its quality and comes to resemble the 30 m SRTM-C distributions (Fig. 8).

The steeper signature of the Quebrada Honda catchment downstream of the knickpoint is apparent in the higher slopes calculated given the same drainage area and curvature bins in Figures 9 and 11, consistent with the steeper baselevel experienced by the downstream catchment. Only the 5 m AW3D5 data provide horizontal L_H results from slope-area plotting (Fig. 9C) within the range (56 m) reported in the literature using this technique (e.g., Montgomery and Foufoula-Georgiou, 1993; Roering et al., 2007; Tarolli and Dalla Fontana, 2009; DiBiase et al., 2012; Grieve et al., 2016a). These values grow with decreasing resolution, even when using the resampled AW3D5 data for the same analysis.

Given the presence of a knickpoint, we expect longer hillslopes in the gently sloped upstream catchment, whereas, our data demonstrate equally long or slightly longer hillslopes downstream. This result may be caused by the choice of bin-width and graphical selection of a rollover value, both subject to user bias. On the other hand, it may be the case that upstream and downstream L_H are similar. In that case, steeper slopes downstream given the same curvature and drainage area (Fig. 9 and 11) would be compensated by greater relief (which our data show is ~200 m greater downstream), rather than longer hillslopes, to maintain steady state of hillslopes with respect to changing baselevels caused by the migrating knickpoint. Additional upstream and downstream differences in curvature related to drainage area are only apparent in the 5 m data (Fig. 10C), where downstream area bins display more planar curvature values than the corresponding upstream area bins. This may indicate that hillslopes downstream are increasingly planar, and thus nearer to the angle of repose (e.g., Roering et al., 1999). The scaling break near zero curvature in Figure 10 may be caused by a change-over from diffusive hillslope processes to advective fluvial processes.

The relative steady state of the upstream and downstream portions of the catchment would be surprising given the presence of a migrating knickpoint, which should affect erosion rates. However, this result may be rectified by the fact that this environment experiences very little rainfall (Bookhagen and Strecker, 2008), and thus rates of fluvial erosion are extremely low, as documented in adjacent areas (Bookhagen and Strecker, 2012). This situation allows hillslopes to adjust to changing baselevels as the knickpoint migrates primarily during short pluvial periods on the Puna (e.g., Trauth et al., 2000).

Although the hillslopes may adjust quickly to the changing baselevel caused by a migrating knickpoint, hilltop curvature should keep pace with erosion for much longer (Hurst et al., 2012).

Attempts to examine this hilltop signal from the 5 m AW3D5 data were complicated by an imperfect setting in the Quebrada Honda. While a number of steep sub-basins can be found downstream of the knickpoint along the steeper trunk reaches, basins 4-6 in Figures 12 and 13 (the largest downstream basins all with areas > 1 km^2) appear to have downstream steepened sections and upstream gently sloped sections. This result is indicated by channel steepness values decreasing moving up-valley from the basin outlets (Fig. 12B). It is possible that the trunk knickpoint signal has yet to reach the higher portions of these catchments given the low rate of fluvial erosion on the Puna. Thus, only a limited number of sharper (more convex) hilltop measurements adjusted to the knickpoint are available to analyze sub-basin transient adjustment, and these may be averaged out when considering all basin values. Another issue may simply be the inability of the 5 m DEM to capture the necessary variability in curvature to assess this signal in the Quebrada Honda. Despite this, slope values do appear to demonstrate coherence with the steeper baselevel (Fig. 13). This same slope analysis carried out on the 10 m TSX/TDX and 30 m SRTM-C also demonstrates the coherence of steeper mean slopes (albeit with ~0.05-0.1 m/m lower magnitude than the slopes calculated from 5 m data) with greater channel steepness, similar to the results of other studies (e.g., DiBiase et al., 2010; Forte et al., 2016).

Taken together, the results indicate the higher quality of the 5 m data in assessing curvature variability and horizontal hillslope lengths. On the other hand, the 10 m TSX/TDX and 30 m SRTM-C perform equally well to the higher resolution data for measuring basin-scale relief and averaged slope values. The potential of high accuracy, satellite derived DEMs in geomorphometry and tectonic geomorphology for exploring the transient response and equilibrium adjustment of large (10-100 km^2) catchments remains high. However, 1-3 m lidar data may still be necessary to assess fine-scale differences in the landscape.

6. Conclusions

We were able to determine the elevation accuracy of the current generation of public access, global 30 m digital elevation models (DEMs) by using a unique, and large areal dataset of differential GPS (dGPS) measurements from the high-elevation, vegetation and cloud free southern Central Andean Plateau (Puna de Atacama). Results indicate the high quality of both the SRTM-C and AW3D30, with fewer no-data voids and fewer step-like hillslope artifacts in the SRTM-C data. Further, we have demonstrated the ASTER products' low quality even after weighted stacking of eight meticulously generated raw L1A DEMs. Our dGPS dataset allowed us to explore the terrain elevation, slope, and aspect biases of the global DEMs. We found little evidence of error biases in the SRTM-C and AW3D30 and only minor aspect biases with the ASTER GDEM2. More future measurements from higher slopes (> 30º) would allow a fuller assessment of the previously described DEM errors on steeper topography, but are limited by dGPS measuring capabilities in the field. The vertical uncertainty of the AW3D5 commercial product was the lowest at < 2 m – strong evidence for the high quality of this newly available 5 m DEM. The 10 m TSX/TDX DEM displayed a wider error distribution, indicating the necessity of stacked scenes for accurate DEM generation for geomorphometry (i.e., likely achieved in the commercial WorldDEM).

Having assessed the accuracy of the DEMs, we chose the highest quality 30 m dataset (SRTM-C) along with the higher resolution 10 m (TSX/TDX) and 5 m (AW3D5) datasets for a geomorphometric analysis of channel profiles and hillslopes in a large (66 km^2) catchment with a clear river knickpoint. These DEMs had similar, low (< 3.5 m) vertical uncertainties, though differences in their resolution may cause differences in derived geomorphic metrics. We show that chi plot analysis of *m/n* values provides comparable results regardless of DEM resolution or chi plot method when applied to the trunk channel alone in this simple setting. Regarding hillslope analyses, the 5 m AW3D5 (25 m^2 per pixel) performs significantly superior to the 10 m TSX/TDX (100 m^2) and 30 m SRTM-C (900 m^2) in assessing characteristic hillslope lengths and curvature, and in capturing a greater range of slopes. On the other hand, the calculation of relief is comparable across DEMs. While slopes provide a metric to track

erosion related to channel steepness regardless of resolution, convex curvature measured on the 5 m DEM is not capable of discerning this signal given complex sub-basin morphology and an inability to capture fine-scale variability at this resolution.

Future work would benefit from a robust algorithm for hilltop curvature mapping from 5-10 m data to better assess changes in curvature at the catchment scale. Overall, our results indicate that the newer generation of 5 m global DEM products can be useful in assessing hillslope parameters at larger scales and lower costs than lidar, but may still be insufficient for fine-scale analysis of hilltop curvature. DEMs acquired by remote sensing technology onboard satellites are reaching better and higher potential for geomorphic analyses including landslide detection and identification of smaller scale features. Despite this improvement, the variability of mountainous landscapes and identification of transient responses in the realm of tectonic geomorphology benefit not only from accuracy, but more importantly, DEM resolution as well.

7. Acknowledgements

8. References

Akaike, H., 1974, A new look at the statistical model identification: IEEE transactions on automatic control, v. 19, no. 6, p. 716-723.

Athmania, D., and Achour, H., 2014, External Validation of the ASTER GDEM2, GMTED2010 and CGIAR-CSI- SRTM v4.1 Free Access

Digital Elevation Models (DEMs) in Tunisia and Algeria: Remote Sensing, v. 6, p. 4600-4620, doi: 10.3390/rs6054600.

Allmendinger, R. W., Jordan, T. E., Kay, S. M., and Isacks, B. L., 1997, The evolution of the Altiplano-Puna plateau of the Central Andes: Annual review of earth and planetary sciences, v. 25, no. 1, p. 139-174, doi: 10.1146/annurev.earth.25.1.139.

Bagnardi, M., González, P. J., and Hooper, A., 2016, High-resolution digital elevation model from tri-stereo Pleiades-1 satellite imagery for lava flow volume estimates at Fogo Volcano: Geophysical Research Letters, 43, doi: 10.1002/2016GL06945.

Becek, K., 2008, Investigation of elevation bias of the SRTM C-and X-band digital elevation models: International archives of the photogrammetry, remote sensing and spatial information sciences, v. 37, p. 105-110.

Berthier, E., Arnaud, Y., Vincent, C., and Remy, F., 2006, Biases of SRTM in high-mountain areas: Implications for the monitoring of glacier volume changes: Geophysical Research Letters, v. 33, no. 8, doi: 10.1029/2006GL025862.

Berthier, E., Arnaud, Y., Kumar, R., Ahmad, S., Wagnon, P., and Chevallier, P., 2007, Remote sensing estimates of glacier mass balances in the Himachal Pradesh (Western Himalaya, India): Remote Sensing of Environment, v. 108, no. 3, p. 327-338, doi: 10.1016/j.rse.2006.11.017.

Berthier, E., and Toutin, T., 2008, SPOT6-HRS digital elevation models and the monitoring of glacier elevation changes in North-West Canada and South-East Alaska: Remote Sensing of Environment, v. 112, no. 5, p. 2443-2454, doi: 10.1016/j.rse.2007.11.004.

Bookhagen, B., and Strecker, M. R., 2008, Orographic barriers, high-resolution TRMM rainfall, and relief variations along the eastern Andes: Geophysical Research Letters, v. 35, no. 6, doi: 10.1029/2007GL032011.

Bookhagen, B., and Strecker, M. R., 2012, Spatiotemporal trends in erosion rates across a pronounced rainfall gradient: Examples from the southern Central Andes: Earth and Planetary Science Letters, v. 327, p. 97-110, doi: 10.1016/j.epsl.2012.02.005.

Burbank, D. W., Leland, J., Fielding, E., Anderson, R. S., Brozovic, N., Reid, M. R. and Duncan, C., 1996, Bedrock incision, rock uplift and threshold hillslopes in the northwestern Himalayas: Nature, v. 379, no. 6565, p. 505-510, doi: 10.1038/379505a0.

Botev, Z. I., Grotowski, J. F., Kroese, D. P., 2010, Kernel density estimation via diffusion: Annals of Statistics, v. 38, no. 5, p. 2916-2957, doi: 10.1214/10-AOS799.

Clubb, F. J., Mudd, S. M., Attal, M., Milodowski, D. T., Grieve, S. W., 2016, The relationship between drainage density, erosion rate, and hilltop curvature: implications for sediment transport processes: Journal of Geophysical Research: Earth Surface, accepted online, doi: 10.10002/2015JF003747.

DiBiase, R. A., Whipple, K. X., Heimsath, A. M., and Ouimet, W. B., 2010, Landscape form and millennial erosion rates in the San Gabriel Mountains, CA: Earth and Planetary Science Letters, v. 289, no. 1, p. 134-144, doi: 10.1016/j.epsl.2009.10.036.

DiBiase, R. A., Heimsath, A. M., and Whipple, K. X., 2012, Hillslope response to tectonic forcing in threshold landscapes: Earth Surface Processes and Landforms, v. 37, no. 8, p. 855-865, doi: 10.1002/esp.3205.

Dietrich, W. E., Bellugi, D. G., Sklar, L. S., Stock, J. D., Heimsath, A. M., and Roering, J. J., 2003, Geomorphic transport laws for predicting landscape form and dynamics, in Prediction in Geomorphology (eds P. R. Wilcock and R. M. Iverson), American Geophysical Union, Washington, D.C., doi: 10.1029/135GM09.

DLR, 2010, DLR SRTM Digital Elevation Models: Online: http://www.dlr.de.

Du, Y., Feng, G., Li., Z, Zhu, J., and Peng, X., 2015, Generation of high precision DEM from TerraSAR-X/TanDEM-X: Chinese Journal of Geophysics, v. 58, no. 9, p. 3089-3102, doi: 10.6038/cjg20150907.

Farr, T. G., Rosen, P. A., Caro, E., Crippen, R., Duren, R., Hensley, S., Kobrick, M., Paller, M., Rodriguez, E., Roth, L., and others, 2007, The shuttle radar topography mission: Reviews of geophysics, v. 45, no. 2, doi: 10.1029/2005RG000183.

Fisher, P. F., and Tate, N. J., 2006, Causes and consequences of error in digital elevation models: Progress in physical Geography, v. 30, no. 4, p. 467-489, doi: 10.1191/0309133306pp492ra.

Fisher, G. B., Bookhagen, B., and Amos, C. B., 2013, Channel planform geometry and slopes from freely available high-spatial resolution imagery and DEM fusion: Implications for channel width scalings, erosion proxies, and fluvial signatures in tectonically active landscapes: Geomorphology, v. 194, p. 46-56, doi: 10.1016/j.geomorph.2013.04.011.

Flint, J., 1974, Stream gradient as a function of order, magnitude, and discharge: Water Resources Research, v. 10, no. 5, p. 969-973.

Forte, A. M., Whipple, K. X., Bookhagen, B., and Rossi, M. W., 2016, Decoupling of modern shortening rates, climate, and topography in the Caucasus: Earth and Planetary Science Letters, v. 449, p. 282-294, doi: 10.1016/j.epsl.2016.06.013.

Gardelle, J., Berthier, E., and Arnaud, Y., 2012, Impact of resolution and radar penetration on glacier elevation changes computed from DEM differencing: Journal of Glaciology, v. 58, no. 208, p. 419-422, doi: 10.3189/2012JoG11J175.

Gonçalves, J., 2008, Orientation And Dem Extraction From ALOS-PRISM Images Using The SRTM-DEM As Ground Control, XXI ISPRS Congress, The International Archives of the Photogrammetry, Remote Sensing and Spatial Information Sciences. Vol. XXXVII. Part B1, p. 1177-1182.

Gorokhovich, Y. and Voustianiouk, A., 2006, Accuracy assessment of the processed SRTM-based elevation data by CGIAR using field data from USA and Thailand and its relation to the terrain characteristics: Remote Sensing of Environment, v. 104, no. 4, p 409-415, doi: 10.1016/j.rse.2006.05.012.

Grieve, S. W., Mudd, S. M., and Hurst, M. D., 2016a, How long is a hillslope?: Earth Surface Processes and Landforms, v. 41, no. 8, p. 1039-1054, doi: 10.1002/esp.3884.

Grieve, S. W., Mudd, S. M., Hurst, M. D., and Milodowski, D. T., 2016b, A nondimensional framework for exploring the relief structure of landscapes: Earth Surface Dynamic, v. 4, no. 2, p. 309-325, doi: 10.5194/esurf-4-309-2016.

Grieve, S. W., Mudd, S. M., Hurst, M. D., Milodowski, D. T., Clubb, F. J., and Furbish, D. J., 2016c, How does grid-resolution modulate the topographic expression of geomorphic processes?: Earth Surface Dynamic, v. 4, no. 3, p. 627-653, doi: 10.5194/esurf-4-627-2016.

Hack, J., 1957, Studies of longitudinal stream profiles in Virginia and Maryland. USGS Report 294B.

Hengl, T., 2006, Finding the right pixel size: Computers & Geosciences, v. 32, no. 9, p. 1283-1298, doi: 10.1016/j.cageo.2005.11.008.

Henkle, J. E., Wohl, E., Beckman, N., 2011, Locations of channel heads in the semiarid Colorado Front Range, USA: Geomorphology, v. 129, no. 3-4, p. 309-319, doi: 10.1016/j.geomorph.2011.02.026.

Hirano, A., Welch, R., and Lang, H., 2003, Mapping from ASTER stereo image data: DEM validation and accuracy assessment: ISPRS Journal of Photogrammetry and Remote Sensing, v. 57, no. 5-6, p. 356-370, doi: 10.1016/S0924-2716(02)00164-8.

Hofton, M., Dubayah, R., Blair, J. B., and Rabine, D., 2006, Validation of SRTM Elevations Over Vegetated and Non-vegetated Terrain Using Medium Footprint Lidar: Photogrammetric Engineering & Remote Sensing, v. 72, no. 3, p. 279-285.

Holzer, N., Vijay, S., Yao, T., Xu, B., Buchroithner, M., and Bolch, T., 2015, Four decades of glacier variations at Muztagh Ata (eastern Pamir): a multi-sensor study including Hexagon KH-9 and Pléiades data: The Cryosphere, v. 9, no. 6, p. 2071-2088, doi: 10.5194/tc-9-2071-2015.

Howard, A. D., Dietrich, W. E., and Siedl, M. A., 1994, Modeling fluvial erosion on regional to continental scales, Journal of Geophysical Research, v. 99, no. B7, p. 13971-13986, doi: 10.1029/94JB00744.

Hurst, M. D., Mudd, S. M., Walcott, R., Attal, M., and Yoo, K., 2012, Using hilltop curvature to derive the spatial distribution of erosion rates: Journal of Geophysical Research: Earth Surface, v. 117, no. F2017, doi: 10.1029/2011JF002057.

Hurvich, C. M., and Tsai, C., 1989, Regression and time series model selection in small samples: Biometrika, v. 76, no. 2, p. 297-307, doi: 10.1093/biomet/76.2.297.

Ijjasz-Vasquez, E. J., and Bras, R. L., 1995, Scaling regimes of local slope versus contributing area in digital elevation models: Geomorphology, v. 12, no. 4, p. 299-311, doi: 10.1016/01695-55X9(50)0012T.

Jaber, W. A., Floricioiu, D., Rott, H., Eineder, M., 2013, Surface elevation changes of glaciers derived from SRTM and TanDEM-X DEM differences, in: 2013 IEEE International Geoscience and Remote Sensing Symposium - IGARSS, p. 1893-1896.

Jarvis, A., Reuter, H. I., Nelson, A., and Guevara, E., 2008, Hole-filled SRTM for the globe Version 4: available from the CGIAR-CSI SRTM 90m Database (http://srtm.csi.cgiar.org).

Kääb, A., 2005, Combination of SRTM3 and repeat ASTER data for deriving alpine glacier flow velocities in the Bhutan Himalaya: Remote Sensing of Environment, v. 94, no. 4, p. 463-474, doi: 10.1016/j.rse.2004.11.003.

Kervyn, M., Goossens, R., Jacobs, P., and Ernst, G.G.J., 2008, Mapping volcano topography with remote sensing: ASTER vs. SRTM: International Journal of Remote Sensing, v. 29, no. 22, p. 6515-6538, doi: 10.1080/01431160802167949.

Kirby, E., and Whipple, K.X., 2012, Expression of active tectonics in erosional landscapes: Journal of Structural Geology, v. 44, p. 54-75, doi: 10.1016/j.jsg.2012.07.009.s

Krieger, G., Zink, M., Bachmann, M., Bräutigam, B., Schulze, D., Martone, M., Rizzoli, P., Steinbrecher, U., Antony, J.W., De Zan, F., Hajnsek, I., Papathanassiou, K., Kugler, F., Rodriguez Cassola, M., Younis, M., Baumgartner, S., López-Dekker, P., Prats, P., and Moreira, A., 2013, TanDEM-X: A radar interferometer with two formation-flying satellites: Acta Astronautica, v. 89, p. 83-98, doi: 10.1016/j.actaastro.2013.03.008.

Kolecka, N., and Kozak, J., 2014, Assessment of the accuracy of SRTM C-and X-Band high mountain elevation data: A case study of the Polish Tatra Mountains: Pure and Applied Geophysics, v. 171, no. 6, p. 897-912, doi: 10.1007/s00024-013-0695-5.

Lague, D., 2014, The stream power river incision model: evidence, theory and beyond: Earth Surface Processes and Landforms, v. 39, no. 1, p. 38-61, doi: 10.1002/esp.3462.

Li, Z., 1988, On the measure of digital terrain model accuracy: The photogrammetric record, v. 12, no. 72, p. 873-877.

Ludwig, R., and Schneider, P., 2006, Validation of digital elevation models from SRTM X-SAR for applications in hydrologic modeling: ISPRS Journal of Photogrammetry and Remote Sensing, v. 60, no. 5, p. 339-358, doi: 10.1016/j.isprsjprs.2006.05.003.

Marschalk, U., Roth, A., Eineder, M., and Suchandt, S., Comparison of DEMs derived from SRTM/X-and C-Band, in Proceedings Geoscience and Remote Sensing Symposium, 2004. IGARSS'04. Proceedings. 2004 IEEE International 2004, Volume 7, IEEE, p. 4531-4534.

METI/NASA/USGS, 2009, ASTER Global DEM Validation Summary Report: METI/ERSDAC, NASA/LPDAAC, USGS/EROS.

Montgomery, D. R., and Foufoula-Georgiou, E., 1993, Channel network source representation using digital elevation models: Water Resources Research, v. 29, no. 12, p. 3925-3934, doi: 10.1029/93WR02463.

Montgomery, D. R., Balco, G., and Willett, S. D., 2001, Climate, tectonics, and the morphology of the Andes: Geology, v. 29, no. 7, p. 579-582, doi: 10.1130/0091-7613(2001)029<0579:CTATMO>2.0.CO;2.

Mudd, S. M., Attal, M., Milodowski, D. T., Grieve, S. W., and Valters, D. A., 2014, A statistical framework to quantify spatial variation in channel gradients using the integral method of channel profile analysis: Journal of Geophysical Research: Earth Surface, v. 119, no. 2, p. 138-152, doi: 10.1002/2013JF002981.

Mukherjee, S., Joshi, P., Mukherjee, S., Ghosh, A., Garg, R., and Mukhopadhyay, A., 2013, Evaluation of vertical accuracy of open source Digital Elevation Model (DEM): International Journal of Applied Earth Observation and Geoinformation, v. 21, p. 205-217, doi: 10.1016/j.jag.2012.09.004.

Neelmeijer, J., Motagh, M., and Bookhagen, B., in review, High-Resolution Digital Elevation Models from Single-Pass TanDEM-X Imagery Over Mountainous Regions: A Case Study for Inylchek Glacier, Central Asia: ISPRS Journal of Phtogrammetry and Remote Sensing.

Neckel, N., Braun, A., Kropáček, J., and Hochschild, V., 2013, Recent mass balance of the Purogangri Ice Cap, central Tibetan Plateau, by means of

differential X-band SAR interferometry: The Cryosphere, v. 7, no. 5, p. 1623-1633, doi: 10.5194/tc-7-1623-2013.

Nuth, C., and Kääb, A., 2011, Co-registration and bias corrections of satellite elevation data sets for quantifying glacier thickness change: The Cryosphere, v. 5, no. 1, p. 271-290, doi: 10.5194/tc-5-271-2011.

Olen, S. M., Bookhagen, B., and Strecker, M. R., 2016, Role of climate and vegetation density in modulating denudation rates in the Himalaya: Earth and Planetary Science Letters, v. 445, p. 57-67, doi: 10.1016/j.epsl.2016.03.047.

Ouimet, W. B., Whipple, K. X., and Granger, D. E., 2009, Beyond threshold hillslopes: Channel adjustment to base-level fall in tectonically active mountain ranges: Geology, v. 37, no. 7, p. 579-582, doi: 10.1130/G30013A.1.

Pandey, P., and Venkataraman, G., 2013, Comparison of DEMs derived from TanDEM-X and SRTM-C for Himalayan terrain, in: 2013 IEEE International Geoscience and Remote Sensing Symposium - IGARSS, p. 322-325.

Passalacqua, P., Belmont, P., Staley, D. M., Simley, J. D., Arrowsmith, J. R., Bode, C. A., Crosby, C., DeLong, S. B., Glenn, N. F., Kelly, S. A., and others, 2015, Analyzing high resolution topography for advancing the understanding of mass and energy transfer through landscapes: A review: Earth-Science Reviews, v. 148, p. 174-193, doi: 10.1016/j.earscirev.2015.05.012

Paul, F., and Haeberli, W., 2008, Spatial variability of glacier elevation changes in the Swiss Alps obtained from two digital elevation models: Geophysical Research Letters, v. 35, no. 21, L21502, doi: 10.1029/2008GL034718

Perron, J. T., and Royden, L., 2013, An integral approach to bedrock river profile analysis: Earth Surface Processes and Landforms, v. 38, no. 6, p. 570-576, doi: 10.1002/esp.3302.

Pike, R., Evans, I., and Hengl, T., 2009, Geomorphometry: a brief guide: Geomorphometry: concepts, software, applications, v. 33, p. 3-30, doi: 10.1016/S0166-2481(08)00001-9.

Racoviteanu, A. E., Manley, W. F., Arnaud, Y., and Williams, M. W., 2007, Evaluating digital elevation models for glaciologic applications: An example from Nevado Coropuna, Peruvian Andes: Global and Planetary Change, v. 59, no. 1-4, p. 110-125, doi: 10.1016/j.gloplacha.2006.11.036.

Rankl, M., and Braun, M., 2016, Glacier elevation and mass changes over the central Karakoram region estimated from TanDEM-X and SRTM/X-SAR digital elevation models: Annals of Glaciology, v. 51, p. 273-281.

Reuter, H., Hengl, T., Gessler, P., and Soille, P., 2009, Preparation of DEMs for geomorphometric analysis: Developments in Soil Science, v. 33, p. 87-120, doi: 10.1016/S0166-2481(08)00004-4.

Rexer, M., and Hirt, C., 2014, Comparison of free high resolution digital elevation data sets (ASTER GDEM2, SRTM v2.1/v4.1) and validation againast accurate heights from the Australian National Gravity Database: Australian Journal of Earth Sciences, v. 61, no. 2, p. 213-226, doi: 10.1080/08120099.2014.884983.

Rignot, E., Echelmeyer, K., and Krabill, W., 2001, Penetration depth of interferometric synthetic-aperature radar signals in snow and ice, Geophysical Research Letters, v. 28, no. 18, p. 3501-3504, doi: 10.1029/2000GL012484.

Rodriguez, E., Morris, C. S., and Belz, J. E., 2006, A global assessment of the SRTM performance: Photogrammetric Engineering & Remote Sensing, v. 72, no. 3, p. 249-260.

Roering, J. J., Kirchner, J. W., and Dietrich, W. E., 1999, Evidence for nonlinear, diffusive sediment transport on hillslopes and implications for landscape morphology: Water Resources Research, v. 35, no. 3, p. 853-870, doi: 10.1029/1998WR900090.

Roering, J. J., Perron, J. T., and Kirchner, J. W., 2007, Functional relationships between denudation and hillslope form and relief: Earth and Planetary Science Letters, v. 264, no. 1, p. 245-258, doi: 10.1016/j.epsl.2007.09.035.

Roering, J. J., Mackey, B. H., Marshall, J. A., Sweeney, K. E., Deligne, N. I., Booth, A. M., Handwerger, A. L., and Cerovski-Darriau, C., 2013, "You are HERE": Connecting the dots with airborne lidar for geomorphic fieldwork: Geomorphology, v. 200, p. 172-183, doi: 10.1016/j.geomorph.2013.04.009.

Rohrmann, A., Strecker, M. R., Bookhagen, B., Mulch, A., Sachse, D., Pingel, H., Alonso, R. N., Schildgen, T. F. and Montero, C., 2014, Can stable isotopes ride out the storms? The role of convection for water isotopes in models, records, and paleoaltimetry studies in the central Andes: Earth and Planetary Science Letters, v. 407, pp. 187-195, doi: 10.1016/j.epsl.2014.09.021.

Rossi, C., Minet, C., Fritz, T., Eineder, M., and Bamler, R., 2016, Temporal monitoring of subglacial volcanoes with TanDEM-X − Application to the 2014–2015 eruption within the Bárðarbunga volcanic system, Iceland: Remote Sensing of Environment, v. 181, p. 186-197, doi: 10.1016/j.rse.2016.04.003.

Scherler, D., Bookhagen, B., Wulf, H., Preusser, F., and Strecker, M. R., 2015, Increased late Pleistocene erosion rates during fluvial aggradation in the

Garhwal Himalaya, northern India: Earth and Planetary Science Letters, v. 428, p. 255-266, doi: 10.1016/j.epsl.2015.06.034.

Schwanghart, W., and Scherler, D., 2014, Short Communication: TopoToolbox 2-MATLAB-based software for topographic analysis and modeling in Earth surface sciences: Earth Surface Dynamics, v. 2, no. 1, p. 1, doi: 10.5194/esurf-2-1-2014.

Shelef, E., and Hilley, G. E., 2013, Impact of flow routing on catchment area calculations, slope estimates, and numerical simulations of landscape development: Journal of Geophysical Research: Earth Surface, v. 118, no. 4, p. 2105-2123, doi: 10.1002/jgrf.20127.

Shortridge, A., and Messina, J., 2011, Spatial structure and landscape associations of SRTM error: Remote Sensing of Environment, v. 115, no. 6, p. 1576-1587, doi: 10.1016/j.rse.2011.02.017.

Smith, B., and Sandwell, D., 2003, Accuracy and resolution of shuttle radar topography mission data: Geophysical Research Letters, v. 30, no. 9, doi: 10.1029/2002GL016643.

Snyder, N. P., Whipple, K. X., Tucker, G. E., and Merritts, D. J., 2000, Landscape response to tectonic forcing: Digital elevation model analysis of stream profiles in the Mendocino triple junction region, northern California: Geological Society of America Bulletin, v. 112, no. 8, p. 1250-1263, doi: 10.1130/0016-7606(2000)112<1250:LRTTFD>2.3.CO;2.

Sun, G., Ranson, K., Kharuk, V., and Kovacs, K., 2003, Validation of surface height from shuttle radar topography mission using shuttle laser altimeter: Remote Sensing of Environment, v. 88, no. 4, p. 401-411, doi: 10.1016/j.rse.2003.09.001.

Tachikawa, T., Kaku, M., Iwasaki, A., Gesch, D. B., Oimoen, M.J., Zhang, Z., Danielson, J. J., Krieger, T., Curtis, B., Haase, J., and others, 2011, ASTER global digital elevation model version 2-summary of validation results: NASA.

Tadono, T., Ishida, H., Oda, F., Naito, S., Minakawa, K., and Iwamoto, H., 2014, Precise global DEM generation by ALOS PRISM: ISPRS Annals of the Photogrammetry, Remote Sensing and Spatial Information Sciences, v. 2, no. 4, p. 71.

Takaku, J., Tadono, T., and Tsutsui, K., 2014, Algorithm development of high resolution global DSM generation by ALOS prism, Geoscience and Remote Sensing Symposium (IGARSS), 2014 IEEE International, p. 4784-4787.

Tarboton, D. G., 2005, Terrain analysis using digital elevation models (TauDEM): Utah State University, Logan.

Tarolli, P., and Tarboton, D., 2006, A new method for determination of most likely landslide initiation points and the evaluation of digital terrain model scale in terrain stability mapping: Hydrology and Earth System Sciences Discussions, v. 10, no. 5, p. 663-677.

Tarolli, P., and Dalla Fontana, G., 2009, Hillslope-to-valley transition morphology: new opportunities from high resolution DTMs: Geomorphology, v. 113, no. 1, p. 47-56, doi: 10.1016/j.geomorph.2009.02.006.

Tarolli, P., 2014, High-resolution topography for understanding Earth surface processes: opportunities and challenges: Geomorphology, v. 216, p. 295-312, doi: 10.1016/j.geomorph.2014.03.008.

Toutin, T., and Cheng, P., 2001, DEM generation with ASTER stereo data: Earth Observation Magazine, v. 10, no. 6, p. 10-13.

Trauth, M. H., Alonso, R. A., Haselton, K. R., Hermanns, R. L., Strecker, M. R., 2000, Climate change and mass movements in the northwest Argentine Andes: Earth and Planetary Science Letters, v. 179, no. 2, p. 243-256, doi: 10.1016/S0012-821X(00)00127-8.

Trisakti, B., and Julzarika, A., 2013, DEM generation from stereo ALOS PRISM and its quality improvement: International Journal of Remote Sensing and Earth Sciences (IJReSES).

Van Niel, T. G., McVicar, T. R., Li, L., Gallant, J. C. and Yang, Q., 2008, The impact of misregistration on SRTM and DEM image difference: Remote Sensing of Environment, v. 112, no. 5, p. 2430-2442, doi: 10.1016/j.rse.2007.11.003.

Vaze, J., Teng, J., and Spencer, G., 2010, Impact of DEM accuracy and resolution on topographic indices: Environmental Modelling and Software, v. 25, no. 10, p. 1086-1098, doi: 10.1016/j.envsoft.2010.03.014.

Wechsler, S., 2007, Uncertainties associated with digital elevation models for hydrologic applications: a review: Hydrology and Earth System Sciences, v. 11, no. 4, p. 1481-1500.

Whipple, K. X. and Tucker, G. E., 1999, Dynamics of the stream-power river incision model: Implications for height limits of mountain ranges, landscape response timescales, and research needs: Journal of Geophysical Research: Solid Earth, v. 104, no. B8, p.17661-17674, doi: 10.1029/1999JB900120.

Wiener, N., 1949, Extrapolation, interpolation, and smoothing of stationary time series, v. 2, MIT Press Cambridge, MA.

Wilson, J. P., 2012, Digital terrain modeling: Geomorphology, v. 137, no. 1, p. 107-121, doi: 10.1016/j.geomorph.2011.03.012.

Wobus, C., Whipple, K. X., Kirby, E., Snyder, N., Johnson, J., Spyropolou, K., Crosby, B., and Sheehan, D., 2006, Tectonics from topography: Procedures, promise, and pitfalls: Geological Society of America Special Papers, v. 398, p. 55-74, doi: 10.1130/2006.2398(04)

Zhang, W., and Montgomery, D. R., 1994, Digital elevation model grid size, landscape representation, and hydrologic simulations: Water resources research, v. 30, no. 4, p. 1019-1028, doi: 10.1029/93WR03553.

9. Appendices

Appendix A. Differential GPS Correction

The collection of high-accuracy dGPS measurements over a large area on the Puna and its margins was conducted during field campaigns from March 2014-2016. Point measurements were collected with two Trimble ProXRS Pathfinder receivers, which logged measurements at 2-5 second intervals in roving modes. Most measurements were made with the unit attached to the roof of the field vehicle while traveling the unpaved roads on the high plateau and its margins. Additional measurements were conducted by fixing the units to backpacks to measure off-road features such as baselevel salar elevations, shorelines, fluvial-lacustrine terraces, and hillslope profiles. The Trimble ProXRS Pathfinder units used in the field rely on GPS L1 and P signals, allowing for centi- to decimeter accuracy in vertical and decimeter accuracy in horizontal measurements. In order to improve measurements to centimeter scale vertical accuracy, daily dGPS files were converted to RINEX format in Trimble Pathfinder Office™ and corrected with RTKLIB open source software for GNSS positioning (http://www.rtklib.com). Real-time kinematic post processing (RTKPOST) of all points was achieved using daily positional data from the International GNSS Service UNSA permanent station in Salta, Argentina (Fig. 1A) (ftp://data-out.unavco.org/pub/rinex/obs). For 333,555 measurements, minimum baseline distance to the UNSA permanent station was 8 km, maximum was 295 km, and the average was 157 km. Additional corrections were applied using global navigation broadcast files, satellite ephemerals, and rapid orbits acquired through NOAA (ftp://www.ngs.noaa.gov/cors/rinex). Positional files output by these tropo- and ionospheric corrections were referenced to the EGM96 / WGS84 datums and converted to merged shapefiles using the GDAL package for geospatial data management in a Python scripting environment (http://www.gdal.org/). Of the 333,555 total raw measurements from 2014-2016, 307,509 points with vertical and horizontal accuracies below 0.5 m were selected for the final dataset. Within this subset, 87.7 % of points have vertical accuracies below 0.2 m and 99.7 % of points had horizontal accuracies below 0.2 m (Fig. A1). The corrected dGPS shapefile contains irregularly spaced information determined by the speed at

which the roving Trimble unit was moving, and were thus rasterized to the DEM of interest using standard GIS tools, taking the average of all measurements within a pixel.
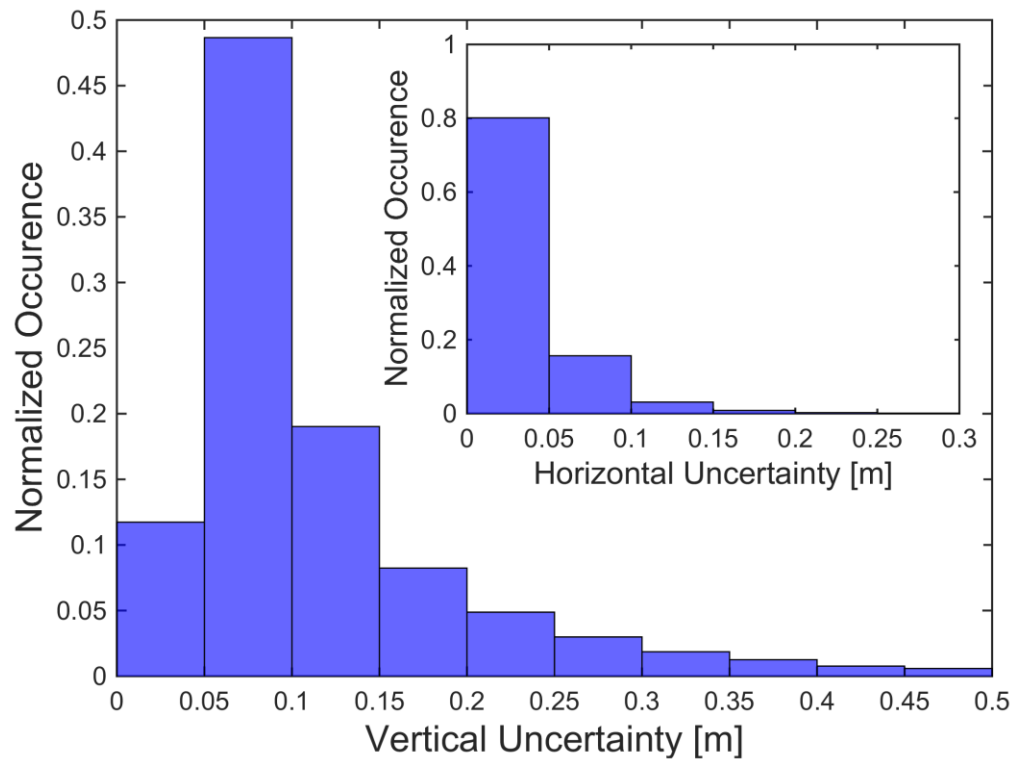

Figure A1. Normalized occurrence of vertical and horizontal (inset) uncertainties of 307,509 dGPS points with uncertainty below 0.5 m selected for DEM accuracy assessments. Correction of original 333,555 raw measurements was achieved using UNSA permanent station in Salta, Argentina. For location of Salta relative to measurements refer to Figure 1A. 87.7 % of points have vertical accuracies below 0.2 m and 99.7 % of points have horizontal accuracies below 0.2 m.

Appendix B. DEM Datasets

Here we provide details on the DEMs presented in Table 1 and used in the main manuscript (SRTM-C 30 m, ASTER GDEM2 30 m, ASTER L1A Stereopair Stack 30 m, AW3D30 30 m, AW3D5 5 m, and TSX/TDX 10 m) along with a number of additional datasets that were not selected for full analysis (SRTMv4.1 90 m, SRTM-X 30 m, RapidEye 12 m, SPOT6 5 m, ALOS PRISM 10 m, TerraSAR-X pairs 10 m, and TerraSAR-X / TanDEM-X pairs processed to 5 m).

SRTM

The SRTM flown aboard the Endeavour Shuttle in February 2000 collected Interferometric Synthetic Aperture Radar (InSAR) at wavelengths of 5.6 cm (C-band) and 3.1 cm (X-band) from 60° N to 56° S. Phase differences between sent and returned signals were used to extract elevation information and generate DEMs for 80 % of the globe free of charge to the scientific community (Farr et al., 2007). C-band returns were used to generate DEMs at resolutions of 1 and 3 arc-seconds (30 and 90 m at the equator, respectively). The 30 m SRTM-C used in the present study was originally developed solely for the United States and only released for other areas in September 2014. Although some data voids persist in the SRTM-C 30 m, it is widely considered the highest quality global DEM publicly available, and thus chosen as the control for co-registration and selection of ground control points for optical DEM generation.

Despite the high quality of the SRTM-C data, RMSE can vary significantly above and below mission standard benchmarks (≤ 16 m; Rodriguez et al., 2006) and should be assessed on an individual basis to analyze terrain (slope and aspect) and land cover (vegetation and snow) effects (e.g., Sun et al., 2003; Berthier et al., 2006; Becek, 2008; Shortridge and Messina, 2011). Furthermore, reports have shown the actual realized resolution of the SRTM datasets is greater than the reported 1 and 3 arc-seconds, caused by final filtering steps to resample and remove noise (Smith and Sandwell, 2003; Tachikawa et al., 2011; Kolecka and Kozak, 2014).

First released in 2003, the hole-filled version of the 90 m SRTM C-band (SRTMv4.1) is available for public download at http://srtm.csi.cgiar.org/ (Jarvis

et al., 2008). The SRTM mission standard vertical RMSE of ≤ 16 m and sub-pixel horizontal accuracy is often surpassed (Rodriguez et al., 2006), and because of this the 90 m SRTMv4.1 continues to be applied to geomorphic studies of regional hillslope and channel morphology (e.g., Forte et al., 2016). The SRTMv4.1 was originally considered in the present study for its global coverage and widespread use, and a complete dataset covering the study area was attained. The vertical uncertainty with respect to 64,515 rasterized dGPS measurements for the SRTMv4.1 was 2.59 ± 5.16 m (mean $\pm$ standard deviation) with a 0.44 % reduction after removal of ±30 m outliers. While this uncertainty was low, and within the range reported in other studies (e.g., Gorokhovich and Voustianiouk, 2006; Rexer and Hirt, 2014), we did not elect to apply further analysis on this 90 m data given the coarse resolution and availability of higher resolution 30 m global DEMs (SRTM-C, ASTER GDEM2, and AW3D30).

Besides the DEMs generated by the SRTM C-band sensor, the SRTM X-band sensor was also used to generate a 1 arc-second (30 m) resolution DEM released in December 2010 by the German Aerospace Center DLR (DLR, 2010). Differences between the SRTM-C and SRTM-X band DEMs are caused by differences in swath coverage: The X-band sensor used single, or maximum double, coverage in cross section, whereas the C-band acquisitions were taken from multiple look directions and incidence angles. Therefore, the C-band achieved better coverage of layover and shadowed areas resulting in a smoother appearance compared with the SRTM-X (Marschalk et al., 2004). Poor quality of the SRTM-X DEM in high relief terrain is caused by terrain slope and aspect as well as the local incidence angle and radar beam geometry. On the other hand, errors in the SRTM-C DEM occur mostly in areas of original data voids that were later filled using interpolation or auxiliary data, and regions with steep slopes (e.g., Ludwig and Schneider, 2006; Kolecka and Kozak, 2014). Although the SRTM-X was noisier upon visual inspection and coverage over the present study area was sparse, we assessed dGPS vertical uncertainty over 20,682 rasterized dGPS measurements. Results indicate a vertical uncertainty of -5.48 $\pm$ 5.32 m with a 0.28 % ±30 m outlier reduction, which is within the range reported for other low vegetated regions (Ludwig and Schneider, 2006) and less

than the uncertainty found in vegetated regions (Kolecka and Kozak, 2014). Because of the lack of coverage over the Quebrada Honda and other parts of the study area, we did not use the SRTM-X for further assessment.

ASTER

Since its launch aboard NASA's Terra spacecraft in December 1999, the ASTER radiometer has collected along-track stereopairs with nadir (Band 3N) and backward (Band 3B) looking near infrared cameras between 83° N and 83° S (Tachikawa et al., 2011). With a base-to-height (B/H) ratio of 0.6 and an optical resolution of 15 m, the ASTER L1A 3N/B scenes are capable of providing stereogrammetric DEMs at spatial resolutions of 30 m with vertical RMSE between 7 and 15 m depending on scene quality and terrain relief (Toutin and Cheng, 2001; Hirano et al., 2003). Eight ASTER L1A stereopairs with variable overlap were collected from the Pocitos Basin for manual generation of 30 m DEMs in the ENVI™ software package. These DEMs were weighted based on their correlation with the SRTM-C and stacked to form a higher quality DEM (ASTER Stack). Ground control points (GCPs) for individual DEM generation were selected from the SRTM-C to provide an absolute vertical reference frame. Mean RMSE of GCPs was high at 7.53 pixels (113 m), likely caused by disagreements in geolocation between ASTER and SRTM (Kääb, 2005). On the other hand, mean tie point (TP) RMSE between identical points selected from the nadir and backward scenes during cross-correlation to extract height information was kept to 0.83 pixels (12 m). Table B1 lists all ASTER L1A scenes along with individual RMSE for the GCPs and TPs.

Table B1. ASTER L1A stereopairs and GCP and TP RMSE values from ENVI™.

ASTER scene full name	Date of capture	Number of GCPs	GCP RMSE (pixels)	Number of TPs	TP RMSE (pixels)
AST_L1A_00300000000000000_20140311171541_22799	September 9, 2009	11	1.66	70	1.14
AST_L1A_0030916200014572 3_20140311171541_22787	September 16, 2000	16	8.16	74	0.71
AST_L1A_00303302002144401_20160215104747_26594	March 30, 2002	9	8.80	115	0.94
AST_L1A_00304072005144209_20160216144251_7801	April 7, 2005	11	8.73	86	0.83
AST_L1A_00308192013144247_20160216144251_7791	August 19, 2013	11	8.58	84	0.85
AST_L1A_00309262015144253_20160216144251_7786	September 26, 2015	10	7.77	80	0.58
AST_L1A_00312092007144229_20160216144251_7796	December 9, 2007	11	8.51	81	0.69
AST_L1A_00312212000145514_20160216144251_7803	December 21, 2000	11	8.01	83	0.92

ALOS

Launched in 2006, the ALOS Panchromatic Remote-sensing Instrument for Stereo Mapping (PRISM) provides another optical satellite source of DEMs (Tadono et al., 2014). With along-track nadir, backward, and forward viewing cameras at 2.5 m resolution providing a maximum B/H ratio of 1, the generation of DEMs at 5 m resolution with vertical and horizontal accuracy < 5 m RMSE is possible (Gonçalves, 2008; Trisakti and Julzarika, 2013). A PRISM tri-stereopair with partial coverage of the Pocitos Basin captured on April 26, 2010 was purchased and processed into a 10 m DEM in PCI-Geomatica™ (which allows bundle adjustment on the three scenes, a feature unavailable in ENVI™). GCP RMSE from the SRTM-C selection process was 0.6 pixels (1.5 m), and TP RMSE between the three scenes was 0.11 pixels (0.3 m). Final PRISM DEM resolution was set to 10 m to avoid persistent errors and artifacts from the 5 m output. Manual editing to remove large artifacts was carried out in the final step of DEM extraction. Additional smoothing in Matlab™ included high-frequency slope and curvature filtering, interpolation of small voids using the surrounding pixel neighborhood, filling of large voids with the SRTM-C resampled to 10 m,

and Wiener (Wiener, 1949) adaptive filtering of the final DEM. Despite multiple attempts at DEM generation and post-processing, the noise remaining in the PRISM tri-stereopair DEM proved insurmountable to geomorphic application.

Similar to the ASTER GDEM endeavor, the ALOS team developed a global DEM (ALOS World 3D 5 m; AW3D5) from autocorrelation and stacking of approximately three million PRISM tri-stereopairs (Tadono et al., 2014; Takaku et al., 2014). Although this high-resolution DEM is only available through commercial purchase, in May 2016 the Japanese Aerospace Exploration Agency (JAXA) released a free 30 m version with terrestrial coverage from 82º N to 82º S (AW3D30; http://www.eorc.jaxa.jp/ALOS/en/aw3d30/). This dataset was downloaded for the entire area covered by the dGPS measurements. Although the AW3D30 contains numerous voids in the study area, coverage over the Quebrada Honda catchment was complete. In addition to the AW3D30, a 580 km^2 clip of the AW3D5 covering the Quebrada Honda was purchased after failure to generate a sufficient DEM for geomorphic application from the raw PRISM tri-stereopair. Mission specifications of < 5 m horizontal and vertical RMSE for the AW3D5 and AW3D30, exceed the SRTM and ASTER mission standards (Tadono et al., 2014), but have yet to be thoroughly assessed.

PRISM tri-stereopair DEMs have been used in previous studies of glacier elevation change (e.g., Holzer et al., 2015) because of their low elevation uncertainty: 3.0 ± 4.52 m over 25,471 dGPS measurements and 0.37 % ±30 m outlier reduction in the present study. However, the mountainous terrain of the Pocitos Basin and its high relief made it difficult to generate a DEM of sufficiently low noise to allow slope and curvature calculation required by geomorphic applications. As in the case of stacking of ASTER L1A stereopair DEMs (ASTER Stack and ASTER GDEM2), the improvement after stacking and averaging of many ALOS PRISM tri-stereopairs is evident in the ALOS World 3D 5 and 30 m DEMs selected for the main manuscript. Therefore, stacking of several manually generated PRISM L1B tri-stereopair DEMs would likely improve accuracy. We do note the tendency of optical DEMs to struggle in flat, low contrast topography (e.g., Berthier and Toutin, 2008), as in the case of the Salar de Pocitos in the present study.

TerraSAR-X / TanDEM-X

The German DLR TerraSAR-X mission launched in 2007 originally collected single pass radar pairs weeks to months apart at various baselines with non-ideal conditions for DEM generation (TSX/TSX pairs). This mission was bolstered in 2010 with the launch of the TanDEM-X satellite flown in tandem with TerraSAR-X to record radar pairs simultaneously and at an optimal baseline for DEM generation (TSX/TDX pairs). Interferometric unwrapping at the sub-wavelength scale of TSX/TDX pairs and stacking of several TSX/TDX pairs was used to generate the 2015 released commercial WorldDEM 10 m dataset, which has a reported vertical accuracy of < 2 m RMSE (Krieger et al., 2013). Here we generated local TSX/TDX DEMs for the Pocitos Basin at 10 m resolution through manual processing using techniques of interferometry. The final DEM was manually edited using edge interpolation of hand-clicked polygons in PCI-Geomatica™ to remove minor artifacts remaining on some hillslopes in the Quebrada Honda catchment.

In addition to the standard 10 m TSX/TDX DEM generation procedure, we attempted to generate 5 m DEMs by using fewer azimuth and range looks but stacking several scenes. The study area is vegetation free and temporal decorrelation is minimal, but unfortunately we did not succeed in generating higher resolution DEMs from TSX/TDX radar pairs of sufficient quality for geomorphic applications. While vertical accuracy for TSX/TDX DEMs was generally low at < 5 m SD, visual inspection revealed many hillslope artifacts, which preclude accurate calculations of slope and curvature. We also generated several 10 m DEMs from TSX/TSX pairs using standard techniques, but because of large temporal differences between scenes, results continued to be of lower quality than the 10 m TSX/TDX DEMs, with SD of vertical uncertainty > 10 m for many of the TSX/TSX DEMs. DEM stacking provided some improvement, but not enough for geomorphic application, given remaining hillslope artifacts.

RapidEye

We received an additional dataset of 10 RapidEye optical satellite scenes with a ground resolution of 6.5 m from the RapidEye Science Archive (Proposal

ID 00195). Given the low incidence angles of the RapidEye scenes (maximum ~15°), we applied bundle adjustment on GCPs and TPs of six overlapping scenes in PCI-Geomatica™ (a feature not included in ENVI™), which provided a maximum B/H ratio of only ~0.2. After numerous attempts at reconfiguring GCPs (final mean RMSE of 3.71 m and 3.77 m in X and Y directions, respectively) and TPs (final mean RMSE of 3.19 m and 3.58 m in X and Y directions, respectively), combining different scenes, testing different output resolutions (12-20 m), and post-processing outputs using smoothing algorithms, we were unable to generate a DEM of sufficient quality for geomorphic application. Final dGPS uncertainty was high at -2.17 ± 12.28 m (n = 22,729), excluding the ±30 m outliers.

SPOT6

Two SPOT6 optical satellite scenes with a ground resolution of 1.5 m were also purchased commercially for the present study. The two scenes were collected at different times of the year (October 27, 2013 and April 13, 2014) with different shadowing, snow cover, and distortion. Although the scene incidence angles were sufficient for DEM generation (~5° and ~26°) we were unable to generate a high resolution (5 m) DEM of sufficient quality in ENVI™ or PCI-Geomatica™, because of moderate snow cover on the highest peaks, shadowing and distortion effects, and temporal distances between scenes. No dGPS uncertainty was calculated because SPOT6 DEM results were dominated by gross artifacts – 1,000+ meter steps or drops in elevation – and large no data voids.

Appendix C. Chi Plot Analysis Parameters

The following details parameters used in the two chi plot techniques. The least-squares maximization method of Perron and Royden (2013) was implemented in TopoToolbox (https://github.com/csdms-contrib/topotoolbox) for Matlab™ (Schwanghart and Scherler, 2014) and the piece-wise fitting method of Mudd et al. (2014) was implemented in the LSDTopoTools (https://github.com/LSDtopotools) software package for Python. Only the trunk channel was selected for chi plot analysis as the inclusion of tributaries led to very noisy results and a large range of m/n calculated depending on dataset and number of tributaries selected. Example plots from the 30 m SRTM-C for both methods are displayed in Figures C1 and C2. For both techniques A_0 in equation (3) was set to 1 km^2. All other parameters are specific only to the piece-wise fitting technique of Mudd et al. (2014).

For the piece-wise fitting, m/n values were tested from 0.35-0.75 with a step size of 0.01. Following parameter sensitivity tests, we calculated m/n with a minimum segment length of 14 nodes, a vertical uncertainty of 20 m (to account for elevation noise in the channel bed), a maximum 100 nodes tested at a time, and 250 Monte Carlo iterations for fitting. Only the mean node skip value was changed between the datasets from 2 to 5 to 10 for the 30, 10, and 5 m DEMs, respectively [see Mudd et al. (2014) for details of each parameter]. The m/n value was found to be most sensitive to vertical uncertainty as indicated by fluctuating values over the full range tested when changing the vertical uncertainty between runs. This is likely caused by over-fitting of the trunk channel with too many individual segments at lower uncertainty values (Mudd et al., 2014). We chose the blanket value of 20 m for vertical uncertainty given the narrow range of DEM resolutions (5-30 m). This value is greater than the SD from dGPS comparison (Table 2), but dGPS measurements occurred mostly in low-slope areas, and not in steep catchments where we expect higher uncertainties on valley bottoms from these satellite derived DEMs.
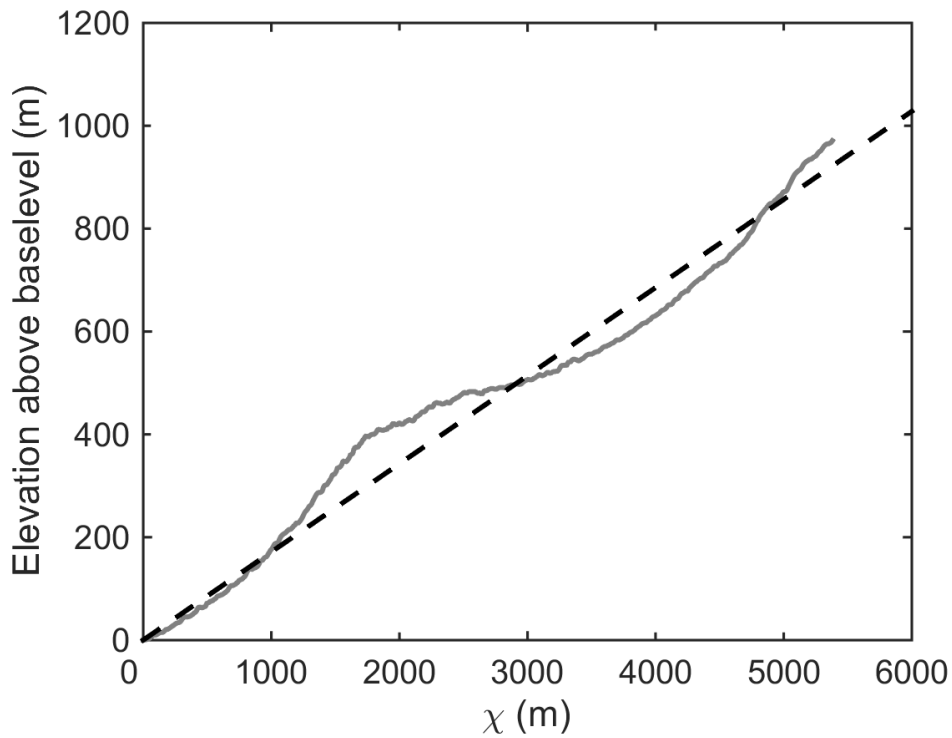
Figure C1. Chi plot analysis for the 30 m SRTM-C using least-squares maximization (Perron and Royden, 2013) implemented in Matlab (TopoToolbox; Schwanghart and Scherler, 2014). Channel is plotted as gray solid line with best-fit linear profile as black dashed line. Note the non-linearity of the channel caused by the knickpoint. Resulting $m/n = 0.52$ with $R^2 = 0.97$.
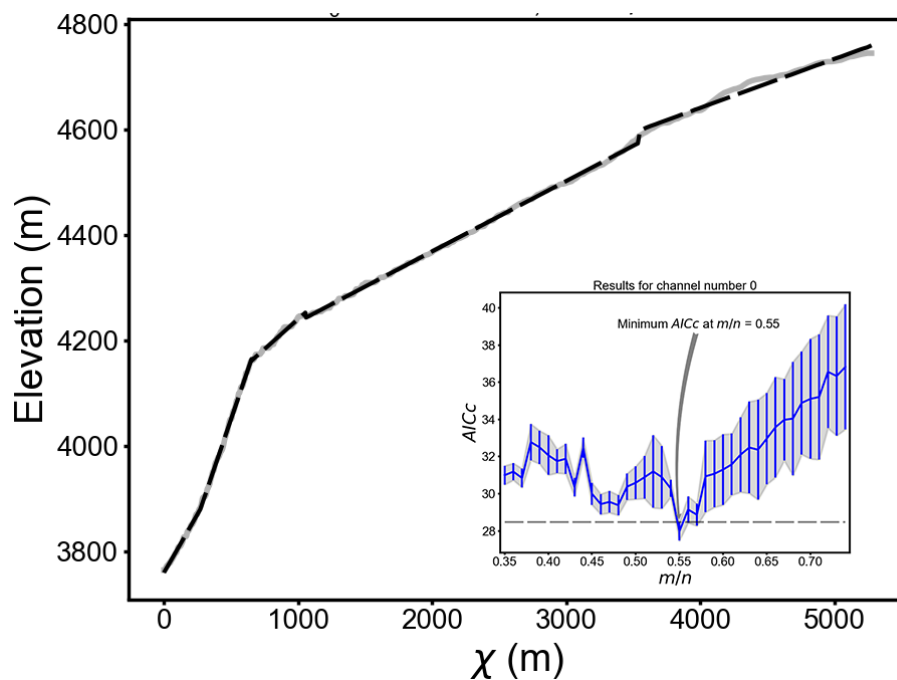

Figure C2. Chi plot analysis for the 30 m SRTM-C using *AICc* minimization (Mudd et al., 2014) implemented in Python (LSDTopoTools). Note the excellent fit (dashed black lines) achieved by breaking the channel (gray line) into segments. Resulting $m/n = 0.55$ at minimum *AICc*, with plausible values of 0.56 and 0.57.

Appendix D. Curvature Calculations

We elected to use Laplacian curvature calculated [by equation (4)] on the raw DEM to preserve variability lost when filtering, following experimentation with Wiener filtering (Wiener, 1949) of DEMs in a 3×3 moving window (Fig. D1). We note that although ridges and valleys become more pronounced using filtered curvature in some of the DEMs (Fig. D1 F-J), the small scale curvature noise is obscured, especially in the 5 m data (Fig. D1 A versus F). Interestingly, the 5 m AW3D5 DEM resampled to 10 m (Fig. D1 C and H) and 30 m (Fig. D1 E and J), both provide better definition of convex (negative) and concave (positive) curvatures compared with the 10 m TSX/TDX (Fig. D1 B and G) and 30 m SRTM-C (Fig. D1. E and J).
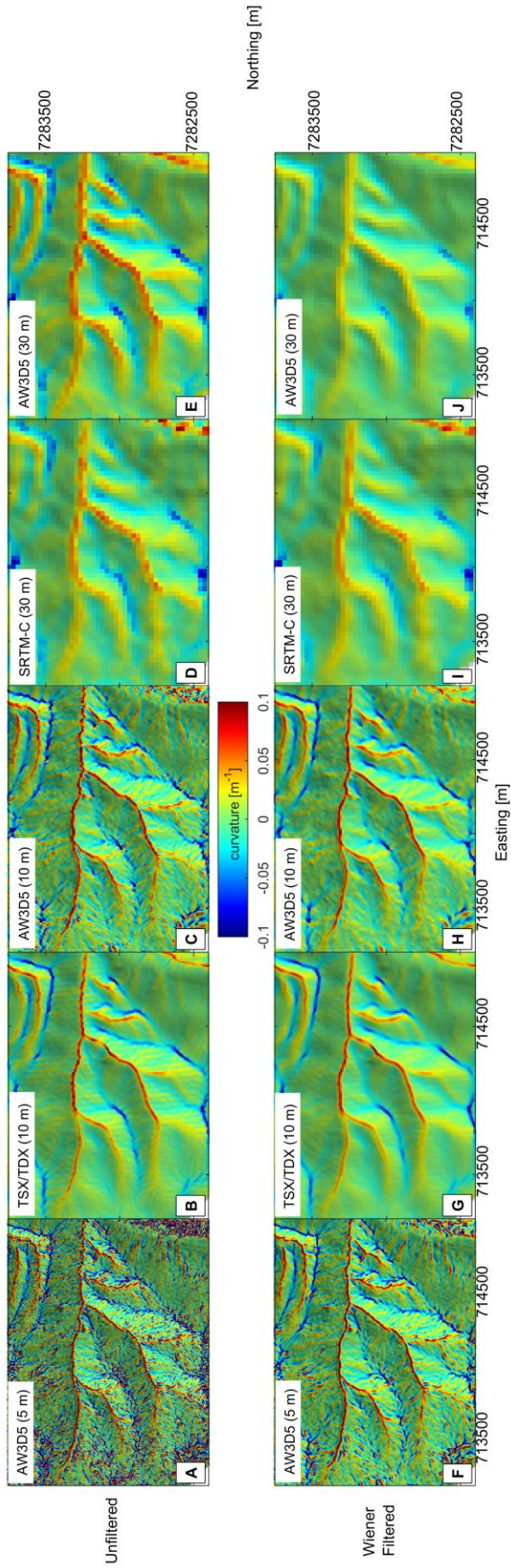
Figure D1. Curvature calculated as Laplacian of elevation [equation (4)] on unfiltered (A-E) and Wiener filtered (F-J) DEMs. See Figure 2D for location.

Appendix E. Inter-basin Variability

Here we present additional plots to complement Figures 12 and 13 of slope and convex curvature distributions separated by sub-basin and plotted as relative distance upstream of outlet with knickpoint location indicated. Figures E1 and E2 for the AW3D5 5 m DEM are the same plots as Figures 12 and 13, however, here box plots are used to represent the full distributions (as opposed to mean and standard deviations). We again note no discernable trend in filtered convex curvature relative to the knickpoint (Fig E1). Furthermore, because of limited slope values calculated on this integer dataset using the D∞ algorithm, the trend in higher slopes downstream of the knickpoint is unclear when plotting median as opposed to mean values, although the higher slopes in basin 8 are still apparent (Fig. E2).
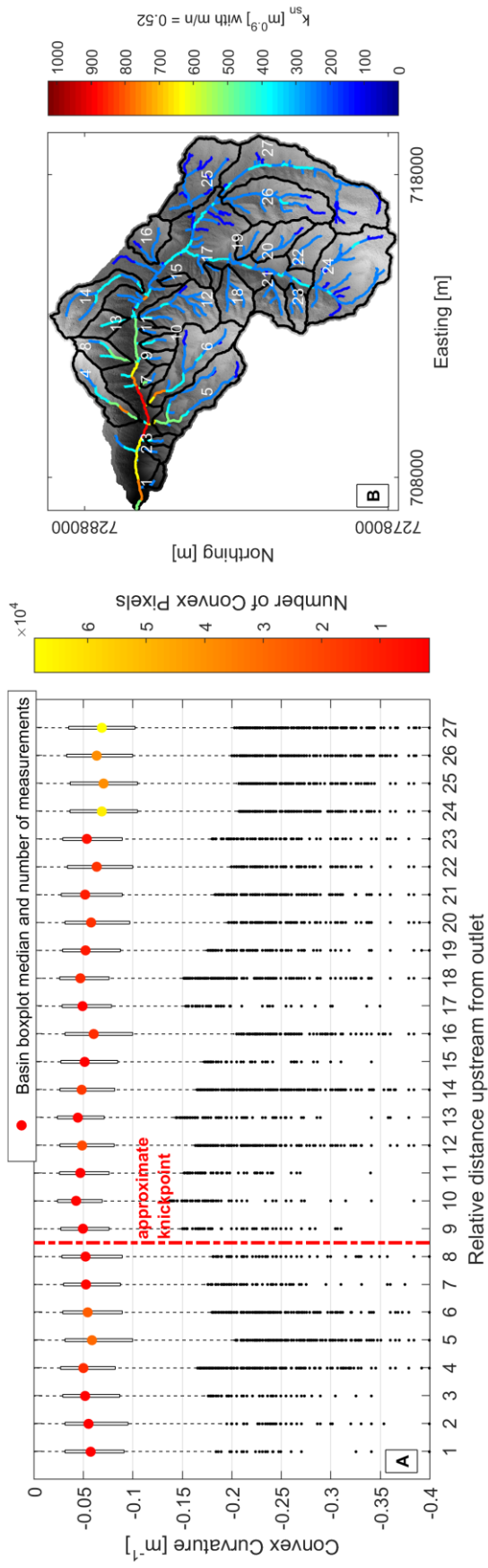
Figure E1. AW3D5 5 m box plot of filtered convex curvature (A) plotted for manually selected sub-basins (B). Channel steepness indicates approximate knickpoint lip location between basins 8 and 9. Number of measurements in each basin indicated by colored circles plotted at the mean value in (A). Curvature calculated as Laplacian of elevation [equation (4)] on unfiltered DEM (cf. Appendix D, Figure D1A). Boxes are plotted at median with quartile ranges (boxes), outlier whiskers, and outlier points indicated. All channels with drainage area > 0.1 km^2 plotted in (B).
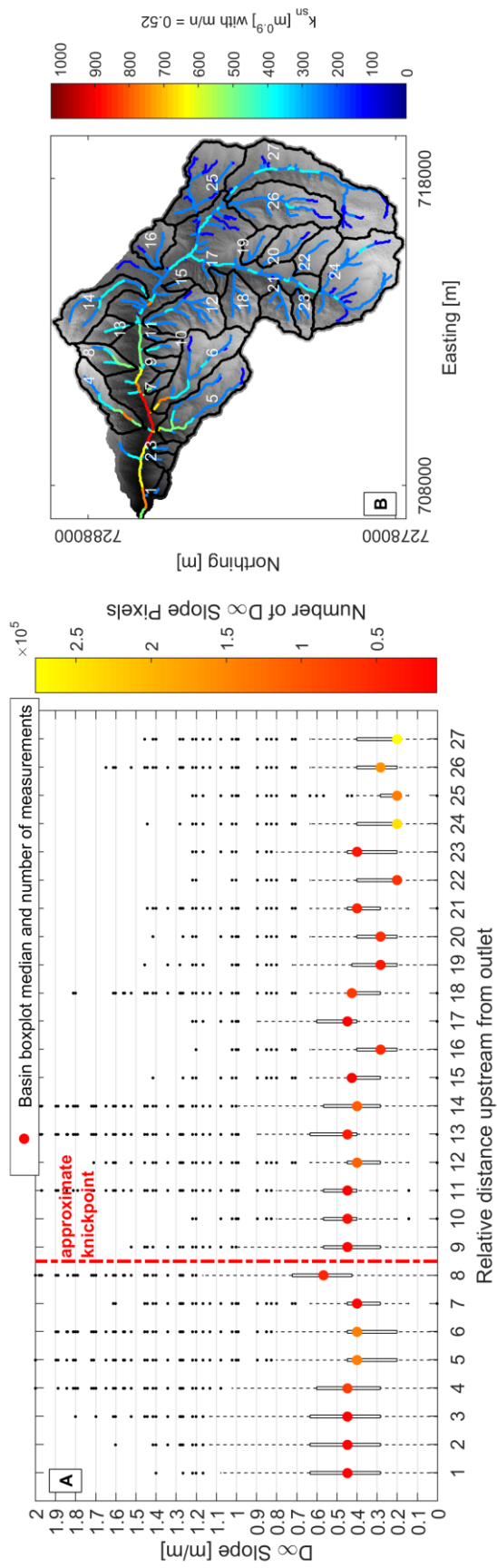
Figure E2. AW3D5 5 m box plot of slopes (A) plotted for manually selected sub-basins (B). Channel steepness indicates approximate knickpoint lip location between basins 8 and 9. Number of measurements in each basin indicated by colored circles plotted at the mean value in (A). Boxes are plotted at median with quartile ranges (boxes), outlier whiskers, and outlier points indicated. Note the stair-cased appearance of the box plots caused by limited slope values calculated on this integer-format DEM. All channels with drainage area > 0.1 km^2 plotted in (B).

Eidesstattliche Erklärung

Hiermit versichere ich an Eides statt, dass ich die vorliegende Masterarbeit ohne fremde Hilfe angefertigt und keine anderen als die angegebenen Quellen und Hilfsmittel benutzt habe. Alle Teile, die wörtlich oder sinngemäß einer Veröffentlichung entstammen, sind als solche kenntlich gemacht. Die Arbeit wurde noch nicht veröffentlicht oder einer anderen Prüfungsbehörde vorgelegt.

Berlin, 12. Oktober 2016

_____

Benjamin Purinton